Eidgenössische Technische Hochschule Zürich
Swiss Federal Institute of Technology Zurich

Characterization of Lithium Niobate for High–Overtone Bulk Acoustic Wave Devices

Angelos Pappas

Supervised by: Dr. Hugo Doeleman, Prof. Yiwen Chu
Hybrid Quantum Systems Group
Laboratory for Solid State Physics, D-PHYS
ETH Zürich

June 24, 2023

Abstract

In the context of circuit Quantum Acoustodynamics there are a numerous of piezoelectric material candidates that could serve as the medium for coupling between the electromagnetic mode of a superconducting circuit and the bulk mechanical mode in a crystal. One of them is Lithium Niobate, for which the high–valued coupling matrix elements make it a potential improvement to the usually–used Aluminum Nitride. However, the measurement of a Lithium Niobate on Sapphire sample showed poor performance, especially in terms of phonon lifetimes. In this work we estimate whether this performance was justified through BeamProp, a python–based simulation software for mechanical mode study and through COMSOL for the coupling rates.

Acknowledgements

I would like to thank Professor Yiwen Chu for giving me the opportunity to be part of the Hybrid Quantum Systems research group and the very nice atmosphere she makes sure to be maintained within the team. Furthermore I would like to thank Dr. Hugo Doeleman for supervising this thesis. He showed great levels of patience and was always open to repeat explanations and answer any question no matter how basic or even dumb they were. There are certainly aspects of his mentorship that I consider valuable and would implement myself in the future.

I would also like to thank the rest of the group with a couple of honorable mentions: Uwe von Lupke, one of the most brilliant people I've met who is also surprisingly kind and funny; Max Drimmer, an incredibly passionate and extremely hard–working person, an amazing teacher with a great span of interests and always up for an adventure.

Finally, a special mention to three people in the group with which I developed a more personal connection: Joost Bus, a fellow Quantum Engineer with which I also had the pleasure of collaborating in a group project, very smart and with a dynamic personality that makes you feel safe, humorous and straightforward with such a bright future ahead of him; Stefano Marti, a person with a heart of gold, a beautiful wide smile to welcome you in the office, with a pure love and excitement for science that makes you motivated, wish we had overlapped for a longer period in the group; Arianne Brooks, one of the most fascinating and awesome people I've met in my life, wouldn't even know where to begin to describe her, but what I do know is that by now I am honored to call her a close friend.

Contents

Chapter 1

Introduction

Quantum technologies represent a rapidly growing field that promises to revolutionize computing, communication, and sensing[1]. These technologies are based on the principles of quantum mechanics, which describe the behavior of matter and energy at the smallest scales. Unlike classical physics, quantum mechanics allows for particles to exist in multiple states simultaneously, leading to new possibilities for data storage, encryption, and processing. As a result, researchers and engineers are exploring new ways to harness quantum properties to create faster, more powerful computers, ultra–secure communication networks, and more sensitive sensors. With the potential to impact nearly every industry, quantum technologies are quickly becoming a major focus of research and development around the world.

There are several different platforms that researchers and engineers are exploring in quantum technologies, each with its own unique advantages and challenges. One of the most promising platforms is superconducting qubits, which use tiny circuits made of superconducting materials to store and manipulate quantum information[2]. Superconducting qubits are highly tunable, allowing for greater control and easier scalability, but they require extremely low temperatures and precise control over their environment to operate effectively. Another platform is trapped ions, which use charged particles held in place by electromagnetic fields to create quantum bits or, for short, qubits[3]. Trapped ions are highly stable and have long coherence times, making them ideal for some applications, but they can be more challenging to scale up and require complex equipment to manipulate. Other platforms being explored include photonics[4], topological qubits[5], and spin qubits[6], each with its own set of advantages and challenges. Despite the challenges, researchers and engineers are making significant progress in developing these platforms, and many believe that a combination of these technologies will ultimately be needed to realize the full potential of quantum technologies.

Hybrid systems are where mechanical resonators could play a role. Mechanical motion couples to many things and so they can couple to a plethora of systems and be the intermediate through which they interact[7]. For example quantum opto– and electromechanical systems interface mechanical motion with the electromagnetic modes of optical resonators and microwave circuits. As a result, mechanical resonators can be used as quantum transducers by converting an excitation in the microwave range to a telecom photon. This has the potential of providing a solution to the scalability of superconducting quantum processors by means of creating quantum networks, a connection between distant processing units, established through optical photons propagating through fibers.

The interaction between acoustics and microwave photons in superconducting circuits, known as Circuit Quantum Acoustodynamics (cQAD)[8][9][10], is a rapidly emerging field on its own. In recent years it has attracted significant attention due to its potential applications in quantum information processing and sensing. Basically, via piezoelectric interactions, mechanical quantum states can be generated through the superconducting qubit. Mechanical resonators have exceptionally long lifetimes even in the GHz regime, with reports in the order of 1 s[11]. Since additionally in this range the acoustic wavelength is much smaller than the electromagnetic one, leading to a small footprint and low cross–talk between them, they are ideal candidates for quantum memories. Furthermore, the qubits can be used to create more special mechanical states, like cat or squeezed states, for which

schemes are being developed for sensing applications [i], like for example for gravitational waves.

The Hybrid Quantum Systems group [ii] focuses on High–overtone Bulk Acoustic Resonators (HBARs), where the phonons are formed within the bulk part of a material. An example is shown in Figure 1.1. For better phonon confinement one side of the resonator is shaped like a dome, leading to a plano–convex cavity geometry. The part *high–overtone* of the term comes from the mechanical standing wave being a high order longitudinal mode, its wavelength is much smaller than the length of the resonator. In order to drive the mechanical wave and to couple a superconducting circuit, a part of the dome is made from a piezoelectric material. The electric field from the circuit causes a harmonic displacement and thus drive of the phonon. In Section 2.2 we will see that the thickness of the piezoelectric material should be half of the phonon wavelength to maximize the coupling between the two parts.

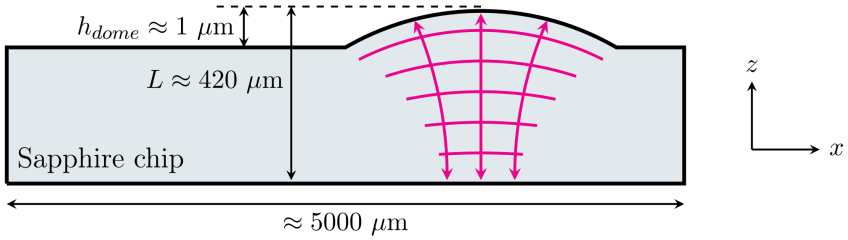

Figure 1.1: Cross section of an HBAR device made out of sapphire. The dome is not to scale with the rest of the bulk. The curved lines under the dome region represent the wavefronts of phonons. Image from [12].

There are alternatives to bulk acoustic resonators like surface acoustic wave devices[13] or micro– and nano–mechanical resonators[14][15]. In these cases however, imperfections at material boundaries yield excess dissipation. In bulk devices surface interactions are reduced by orders of magnitude and thus higher quality factors can be achieved[16].

1.1. Outline

This thesis consists of four more chapters. Chapter 2 gives a background about cQAD. Chapter 3 introduces BeamProp, which is one of the simulation tools the group is using, and then reports on additional work done in BeamProp and in COMSOL. The results of those simulations are presented in chapter 4. Finally chapter 5 contains information regarding the experimental setup used in cQAD along with the results of specific devices that were measured during this project.

[i] https://mqsens.eu
[ii] https://hyqu.ethz.ch/

Theoretical Background

This chapter contains two sections. The first is about the quantization of mechanical modes and is contained for two reasons: usually graduate–level quantum courses deal only with the quantization of electromagnetic modes, and furthermore it is a prerequisite for the second section. The latter has to do with the piezoelectric coupling derivation, which is one of the fundamental quantities in cQAD as in order to be in the strong–coupling regime we need it to exceed the loss rates of the mechanical and the electromagnetic modes.

2.1. Mechanical modes

Let us first cover some more fundamental concepts, mainly based on chapters 4, 5 and 7 of [17], in order to properly introduce mechanical modes. We consider two points within a solid, P and Q, at initial positions $\underline{r}$ and $\underline{r}+\Delta\underline{r}$ respectively, in the limit where they are infinitesimally close. Under deformation these points move to positions $\underline{r'}$ and $\underline{r'}+\Delta\underline{r'}$, as shown in Figure 2.1. If we want to see how their displacements correlate to their initial relative position then the Taylor expansion of $\underline{u}(\underline{r}+\Delta\underline{r})$ about $\underline{u}(\underline{r})$ gives:

$$u_i(\underline{r}+\Delta\underline{r}) = u_i(\underline{r}) + \sum_{j=1}^{3} \frac{\partial u_i}{\partial x_j}\Delta r_j + \text{higher order terms.} \tag{2.1}$$

By dropping the higher order terms we get:

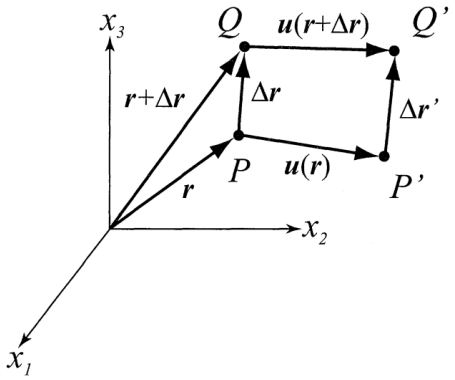

Figure 2.1: Positions of two points within a solid before and after deformation. Image from [17].

$$\Delta u_i = \sum_{j=1}^{3} \frac{\partial u_i}{\partial x_j}\Delta r_j \tag{2.2}$$

and so through the set of partial derivatives, $^{\partial u_i}/_{\partial x_j}$, which are functions of position $\underline{r}$ within the body, we can calculate the strain-induced relative displacement of any two points by integrating these derivatives in the appropriate way. These derivatives can be assembled into a tensor, $\underline{\underline{D}} = \nabla\underline{u}$, which can be broken down into a symmetric and an anti–symmetric

part:

$$\underline{\underline{D}} = \underline{\underline{S}} + \underline{\underline{\Omega}} \qquad \text{with} \qquad \underline{\underline{S}} = \frac{1}{2}(\nabla \underline{u} + (\nabla \underline{u})^T) \qquad \text{and} \qquad \underline{\underline{\Omega}} = \frac{1}{2}(\nabla \underline{u} - (\nabla \underline{u})^T). \tag{2.3}$$

Two examples are shown in Figure 2.2. Displacement $\underline{u}(x, y, z) = [0.3x, 0, 0]$ leads to

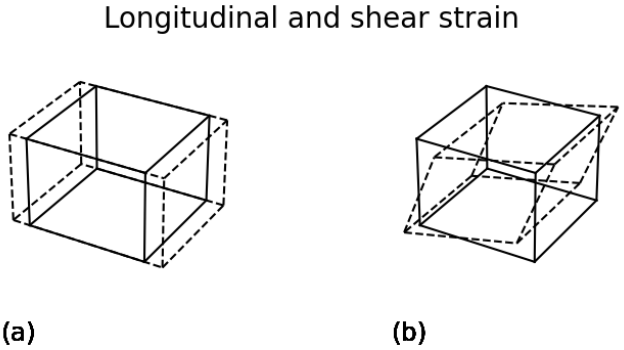

Figure 2.2: Original shapes are drawn with solid lines and deformed solids with dashed. (a) Longitudinal strain, $\underline{u}(x, y, z) = [0.3x, 0, 0]$. (b) Shear strain, $\underline{u}(x, y, z) = [0.3z, 0, 0.3x]$.

a longitudinal strain where only the element S_{11} of $\underline{\underline{S}}$ is non–zero, while for $\underline{u}(x, y, z) = [0.3z, 0, 0.3x]$ the non–zero elements of the symmetric strain tensor are S_{13} and S_{31}.

For a solid of density ρ, under stress $\underline{\underline{T}}$ and body forces $\underline{f}(\underline{r})$ the description of the dynamics comes from Newton's second law as:

$$\nabla \underline{\underline{T}}(\underline{r}) + \underline{f}(\underline{r}) = \rho \frac{\partial^2 \underline{u}}{\partial t^2}. \tag{2.4}$$

Under small displacements most materials have a linear stress–strain relation, described by the stiffness tensor, $\underline{\underline{\underline{c}}}$, as:

$$T_{ij} = c_{ijlm} S_{lm}. \tag{2.5}$$

In that case, if we also ignore the body forces, then equation 2.4 gives:

$$c_{ijlm} \frac{\partial^2 u_l}{\partial x_j \partial x_m} = \rho \frac{\partial^2 u_i}{\partial t^2}. \tag{2.6}$$

2.1.1. Christoffel equation

If we focus on equation 2.6, which looks like a wave equation, and consider a solution of a plane–wave form:

$$\underline{u}(\underline{r}, t) = U_0 e^{i(\underline{q} \cdot \underline{r} - \omega t)} \hat{\epsilon}, \tag{2.7}$$

with $\underline{q}$ the wavevector and $\hat{\epsilon}$ the polarization, then this leads to:

$$\rho \omega^2 \epsilon_i = \sum_{j,l,m=1}^{3} c_{ijlm} \hat{q}_j \hat{q}_m \epsilon_l, \tag{2.8}$$

with $\hat{q}_j = \underline{q} \cdot \hat{e}_j / |\underline{q}|$, the normalized wavevector components.

From now on we will use the *Einstein summation notation*, where repeating indices indicate summation over that index. For example, in the above equation there are three repeating indices (j, l and m) and using this notation it is written as:

$$\rho \omega^2 \epsilon_i = c_{ijlm} \hat{q}_j \hat{q}_m \epsilon_l. \tag{2.9}$$

For future equations, unless stated otherwise, the Einstein notation is the default.

The above can be transformed into a characteristic equation by defining the Christoffel tensor with elements:

$$D_{il} = \frac{1}{\rho} c_{ijlm} \hat{q}_j \hat{q}_m \tag{2.10}$$

From that we get the *Christoffel equation*:

$$D_{il}\epsilon_l = \upsilon^2 \epsilon_i. \tag{2.11}$$

As a result, for each $\hat{q}$ this second–rank tensor will have three eigenvalues, υ_μ and three eigenvectors, $\hat{\epsilon}_\mu(\hat{q})$. The latter correspond to three polarizations of plane waves and the former to their phase velocities. One of these eigenvectors is going to be the one closest to being parallel to $\hat{q}$ and is the one we call *quasi–longitudinal* wave, while the other two are the *quasi–transverse*.

For an elastic material one can solve equation 2.11 for all directions and define a surface in q–space with all the points coming from the endpoints of vectors $\underline{\upsilon} = \upsilon(\underline{q})\hat{q}$. This is the *velocity surface*. Another useful representation though is the inverse of the velocity surface, for which the points come from the vectors $1/\upsilon(\underline{q})\hat{q}$. This is what we call the *slowness surface* and it has the following interesting properties:

- it has the same shape as a surface of constant ω in q–space
- the Poynting vector and thus the direction of energy propagation points along the normal to the slowness surface.

2.1.2. Quantization

In an elastic material a solution of equation 2.6 that has the form:

$$\underline{u}(\underline{r}, t) = u_0 e^{-i\omega t} \underline{h}(\underline{r}) + \text{c.c.} = u_0(t)\underline{h}(\underline{r}) + \text{c.c.} \tag{2.12}$$

where $\underline{h}(\underline{r})$ is a function that contains the spatial dependence and polarization of the displacement, which is assumed to be normalized, $\int |\underline{h}(\underline{r})|^2 \, dV = 1$, is what we call a *normal mode*. The units of the terms are $[\underline{h}(\underline{r})] = \mathrm{m}^{-3/2}$ and $[u_0] = \mathrm{m}^{5/2}$. The actual displacement will be the real part of equation 2.12.

As in the case of electromagnetic modes in quantum optics, here as well the quantization is derived through the form of the Hamiltonian of the system which is given by:

$$\begin{aligned}
H &= T + V \\
&= \int \frac{1}{2}\rho \frac{\partial u_i}{\partial t}\frac{\partial u_i^*}{\partial t}\, dV + \underbrace{\int \frac{1}{2} c_{ijlm} \frac{\partial u_i}{\partial x_j}\frac{\partial u_l}{\partial x_m}\, dV}_{\text{applying divergence theorem}} \\
&= \frac{1}{2}\rho\omega^2 |iu_0(t) - iu_0^*(t)|^2 \int |\underline{h}(\underline{r})|^2 \, dV + \underbrace{\frac{1}{2}\int n_j c_{ijlm} u_i \frac{\partial u_l}{\partial x_m}\, dS}_{\text{assuming no energy leaves the system}} \\
&\quad - \frac{1}{2}\int u_i c_{ijlm} \frac{\partial^2 u_l}{\partial x_j \partial x_m}\, dV \\
&= \frac{1}{2}\rho\omega^2 |iu_0(t) - iu_0^*(t)|^2 + 0 - \frac{1}{2}\rho \int u_i \frac{\partial^2 u_i}{\partial t^2}\, dV \\
&= \frac{1}{2}\rho\omega^2 |iu_0(t) - iu_0^*(t)|^2 + 0 + \frac{1}{2}\rho\omega^2 \int u_i^2 \, dV \\
&= \frac{1}{2}\rho\omega^2 |iu_0(t) - iu_0^*(t)|^2 + 0 + \frac{1}{2}\rho\omega^2 \int |u_i|^2 \, dV \\
&= \frac{1}{2}\rho\omega^2 |iu_0(t) - iu_0^*(t)|^2 + 0 + \frac{1}{2}\rho\omega^2 |u_0(t) + u_0^*(t)|^2 \int |\underline{h}(\underline{r})|^2 \, dV
\end{aligned} \tag{2.13}$$

$$= \frac{1}{2}\rho\omega^2(|iu_0(t) - iu_0^*(t)|^2 + |u_0(t) + u_0^*(t)|^2)$$
$$= 2\rho\omega^2|u_0(t)|^2 \tag{2.14}$$

with n_j the j–th element of a unit vector that is normal to the surface around the mode's volume. We also used the fact that the displacement is a real number to write $u_i^2 = |u_i|^2$. If we define the conjugate variables:

$$q = u_0(t) + c.c. \qquad p = -i\omega\rho u_0(t) + c.c. \tag{2.15}$$

then 2.13 gives:

$$H = \frac{p^2}{2\rho} + \frac{1}{2}\rho\omega^2 q^2 \tag{2.16}$$

which has the form of the mechanical resonator Hamiltonian and can be quantized. The above operators can thus be written in terms of the ladder operators $\hat{b}$ and $\hat{b}^\dagger$ as:

$$\hat{q} = \sqrt{\frac{\hbar}{2\rho\omega}}(\hat{b} + \hat{b}^\dagger) \qquad \hat{p} = -i\sqrt{\frac{\rho\hbar\omega}{2}}(\hat{b} - \hat{b}^\dagger). \tag{2.17}$$

The quantum displacement operator can be written as:

$$\hat{\underline{u}}(\underline{r}, t) = \sqrt{\frac{\hbar}{2\rho\omega}}\underline{h}(\underline{r})\hat{b}(t) + H.c. \tag{2.18}$$

and the quantum strain tensor:

$$\hat{\underline{S}}(\underline{r}, t) = \sqrt{\frac{\hbar}{2\rho\omega}}\nabla\underline{h}(\underline{r})\hat{b}(t) + H.c.\,. \tag{2.19}$$

The multimode extension of this derivation gives:

$$\hat{\underline{u}}(\underline{r}, t) = \sum_{m=1}^{M}\sqrt{\frac{\hbar}{2\rho\omega}}\underline{h}_m(\underline{r})\hat{b}_m(t) + H.c. \tag{2.20}$$

$$\hat{\underline{S}}(\underline{r}, t) = \sum_{m=1}^{M}\sqrt{\frac{\hbar}{2\rho\omega}}\nabla\underline{h}_m(\underline{r})\hat{b}_m(t) + H.c.\,. \tag{2.21}$$

2.2. Piezoelectric coupling

The above treatment has been applied for the quantization of electromagnetic fields, as found in every Quantum Optics textbook like [18], where we find the electric field operator:

$$\hat{\underline{E}}(\underline{r}, t) = -i\sqrt{\frac{\hbar\omega}{2\epsilon_0}}\underline{f}(\underline{r})\hat{a}(t) + H.c., \tag{2.22}$$

which for the multimode case would respectively give:

$$\hat{\underline{E}}(\underline{r}, t) = \sum_{n=1}^{N}(-i\sqrt{\frac{\hbar\omega_n}{2\epsilon_0}}\underline{f}_n(\underline{r})\hat{a}(t) + H.c.). \tag{2.23}$$

In an experiment that includes an electromagnetic device and a mechanical device the total energy of the system would be the sum of the two sub–parts for most materials. If

however, like the case of cQAD, there is a piezoelectric material present that is no longer the case. The piezoelectric relations in stress–charge form, meaning with strain and electric field as independent variables give[19]:

$$\begin{pmatrix} \underline{\underline{T}} \\ \underline{D} \end{pmatrix} = \begin{pmatrix} \underline{\underline{\underline{\underline{c}}}}_E & -\underline{\underline{\underline{e}}}^T \\ \underline{\underline{\underline{\underline{c}}}}_E & \underline{\underline{\epsilon}}_S \end{pmatrix} \begin{pmatrix} \underline{\underline{S}} \\ \underline{E} \end{pmatrix} \tag{2.24}$$

where $\underline{\underline{\epsilon}}_S$ is the permittivity at constant stress, $\underline{\underline{\underline{\underline{c}}}}_E$ the stiffness tensor at constant electric field and $\underline{\underline{\underline{e}}}$ the piezoelectric coupling tensor.

The piezoelectric coupling is calculated through the internal energy density of the whole system, U, with differential form:

$$dU = \underline{\underline{T}} \cdot d\underline{\underline{S}} - \underline{E} \cdot d\underline{D}. \tag{2.25}$$

If, as in equation 2.24, we want to have the strain and electric field as the independent variables, then a more convenient quantity is:

$$G \coloneqq U - \underline{E} \cdot \underline{D}, \tag{2.26}$$

which from 2.24 gives:

$$\begin{aligned} dG &= \underline{\underline{T}} \cdot d\underline{\underline{S}} - \underline{D} \cdot d\underline{E} \\ &= (\underline{\underline{\underline{\underline{c}}}}_E \underline{\underline{S}} - \underline{\underline{\underline{e}}}^T \underline{E}) \cdot d\underline{\underline{S}} - (\underline{\underline{e}}\,\underline{\underline{S}} + \underline{\underline{\epsilon}}_S \underline{E}) \cdot d\underline{E}. \end{aligned} \tag{2.27}$$

In Voigt notation the above leads to:

$$\begin{aligned} U &= G + ED \\ &= \frac{1}{2} \sum_{i,j=1}^{6} c_{ij} S_i S_j - 2 \sum_{\alpha,j=1}^{3,6} e_{\alpha j} E_\alpha S_j + \frac{1}{2} \sum_{\alpha,\beta=1}^{3} \epsilon_{\alpha\beta} E_\alpha E_\beta. \end{aligned} \tag{2.28}$$

Apart from the independent parts there is also the interaction Hamiltonian:

$$\hat{H}_{int}/\hbar = \frac{1}{\hbar} \int \sum_{\alpha,j=1}^{3,6} e_{\alpha j} \hat{E}_a \hat{S}_j \, dV \sim g \hat{a}^\dagger \hat{a} + H.c. \tag{2.29}$$

and so in the end, from 2.21, 2.23 and 2.29 we get the coupling term between an electromagnetic mode at frequency ω_n and a mechanical mode at ω_m to be:

$$g_{nm} = \frac{1}{2} \sqrt{\frac{\omega_n}{\rho \epsilon_0 \omega_m}} \int (f_n^i)^* e_{ijk} (\nabla \underline{h}_m)^{ij} \, dV. \tag{2.30}$$

The last term in the above integral is the strain of the mode of interest which, as shown in Figure 1.1, has a certain spatial distribution in the x–y plain (depending on the order of the excited mode) and is sinusoidal in z, with wavelength λ. During the integration the sinusoidal part will be initially maximized if the length of the piezoelectric is $\lambda/2$. Different piezoelectric materials have different phase velocities and so the targeted thickness of the piezoelectric layer will vary.

In order to increase the coupling rate one could try and shape the electric field so that it has high value inside the piezoelectric material volume and form that overlaps well with the mechanical mode of interest or look into materials with high piezoelectric tensor values. The case for Lithium Niobate has been for the latter.

Simulation Tools

In this chapter we introduce the tools that were developed/used in order to investigate topics related to the lifetime and the coupling rates of our HBARs. More specifically the questions we want to answer are:

1. Do reflections limit the lifetimes in $LiNbO_3$ HBARs?
2. For which radius of curvature are lifetimes affected?
3. Does polarization conversion form a significant source of loss for our HBARs?
4. What coupling rates can we expect with $LiNbO_3$ HBARs and how do those compare to the couplings to unwanted modes?

For the first three of those questions we use BeamProp and for the last COMSOL. Initially the BeamProp algorithm is described, which along with the *1D–displacement approximation* were already implemented by the group before the start of this thesis.

3.1. BeamProp

3.1.1. BeamProp Algorithm

BeamProp is a software package used to simulate the propagation of acoustic modes inside a bulk acoustic resonator. The basic concept is representing the beam as an angular spectrum of plane waves propagating in a direction centered about the symmetry axis of the HBAR (usually this is considered the z–axis)[20]. Since there are three slowness surfaces there are three plane wave solutions for each propagation direction and the general solution of this representation has the form:

$$\underline{u}(x,y,z,t) = (\frac{1}{2\pi})^3 \int_{-\infty}^{\infty} d\omega \int_{-\infty}^{\infty} dk_x \int_{-\infty}^{\infty} dk_y \sum_{n=1}^{3} \phi^n(k_x,k_y,\omega)\hat{d}^n(\frac{k_x}{\omega},\frac{k_y}{\omega})e^{i(\omega t - k_x x - k_y y - k_z^n z)} \tag{3.1}$$

where n indexes the three slowness surfaces, $\hat{d}^n(\frac{k_x}{\omega},\frac{k_y}{\omega})$ is the polarization vector for the plane wave propagating along (k_x,k_y,k_z^n), with k_z^n determined by the corresponding slowness surfaces and $\phi^n(k_x,k_y,\omega)$ the amplitude for each polarization.

The goal is to find the response to a harmonic input of the form $\underline{u}(x,y,z,t) = \underline{u}(x,y,z)e^{i\Omega t}$. For that, we perform the following steps, described in [16]:

1. We consider an initial displacement on the flat side of the HBAR, $\underline{u}_0(x,y,z=0)$
2. and find the Fourier transform of that,
   $\underline{H}(k_x,k_y,\Omega) = \int_{-\infty}^{\infty} dt \int_{-\infty}^{\infty} dx \int_{-\infty}^{\infty} dy\, \underline{u}_0(x,y,z=0)e^{i(\omega t - k_x x - k_y y - k_z^n z)}$.
3. From the knowledge of the slowness surfaces around the propagation direction, meaning $k_z^n = q_z^n\Omega = f(k_x/\Omega, k_y/\Omega)$ around $\hat{n} = [0,0,1]$ and the corresponding polarization vectors, $\hat{d}^n$, the initial displacement can be decomposed into quasi–longitudinal and quasi–transverse plane waves with amplitudes ϕ^n, where

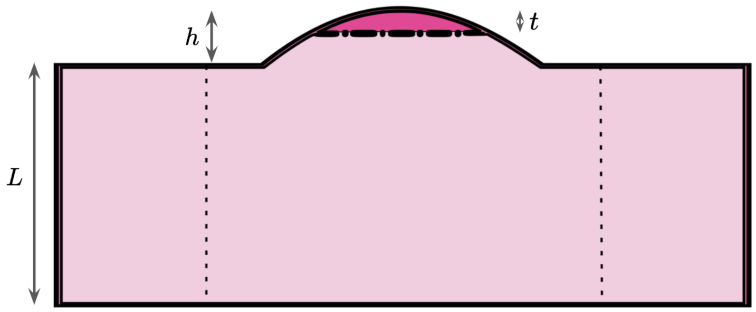

Figure 3.1: Example of a 2D cut of the 3D geometry defined in BeamProp. The bulk material (light pink) length is L, the dome has a circular shape with maximum height h and maximum piezoelectric (dark pink) thickness t. The dotted lines indicate the region out of which we introduce losses.

$$\phi^{n=1}(k_x, k_y, \Omega) = \frac{\{\underline{H}\cdot\hat{d}^1[1-(\hat{d}^2\cdot\hat{d}^3)^2] + \underline{H}\cdot\hat{d}^2[(\hat{d}^1\cdot\hat{d}^3)(\hat{d}^2\cdot\hat{d}^3) - \hat{d}^1\cdot\hat{d}^2] + \underline{H}\cdot\hat{d}^3[(\hat{d}^1\cdot\hat{d}^2)(\hat{d}^3\cdot\hat{d}^2) - \hat{d}^1\cdot\hat{d}^3]\}}{\{1+2(\hat{d}^1\cdot\hat{d}^2)(\hat{d}^2\cdot\hat{d}^3)(\hat{d}^3\cdot\hat{d}^1) - (\hat{d}^1\cdot\hat{d}^2)^2 - (\hat{d}^1\cdot\hat{d}^3)^2 - (\hat{d}^2\cdot\hat{d}^3)^2\}}. \tag{3.2}$$

Similarly ϕ^2 and ϕ^3 are obtained by permutation of indices. Once these coefficients are calculated, the field at $z = L$ is found using equation 3.1.

4. For the propagation inside the dome we consider $\underline{u}(x, y, z = L)$ with a position–dependent phase shift that corresponds to the beam propagating inside the curved surface and back (dome) in real space. The reflected field is thus given as:

$$\begin{bmatrix} u_x\prime(x,y,z=L) \\ u_y\prime(x,y,z=L) \\ u_z\prime(x,y,z=L) \end{bmatrix} = \begin{bmatrix} u_x(x,y,z=L)e^{i2k_{t1}h_{t1}(x,y)} \\ u_y(x,y,z=L)e^{i2k_{t2}h_{t2}(x,y)} \\ u_z(x,y,z=L)e^{i2k_l h_l(x,y)} \end{bmatrix}. \tag{3.3}$$

In this step we consider propagation towards the $[0, 0, 1]$ direction. Let us assume that the slow–transverse surface is the one that is mainly x–polarized in that direction, hence k_{t1} is used for the calculation of $u_x\prime$ and the phase velocity of interest is $v_{ph,x,bulk}$. Looking into Figure 3.1, since we have propagation in two materials, in order to account for the different phase velocities we define the effective length of the dome as $h_{t1}(x, y) = h(x, y) - t(x, y) + v_{ph,x,bulk}/v_{ph,x,piezo}t(x, y)$. Similarly we get the remaining terms of the above equation.

In addition we introduce losses by multiplying the field outside the dome region, indicated by the doted lines in Figure 3.1, with a number $0 \leq \beta \leq 1$. This dissipation region starts a few μm outside the dome, $\beta = 1$ at the dotted line and is decreasing as a cos^2 as we approach the edge, where $\beta = 0$. Then, steps 1–4 are repeated for propagation to the other side of the crystal and in the end, starting from $\underline{u}_0(x, y, z = 0)$ we get the displacement field after one propagation through the crystal $\underline{u}_1(x, y, z = 0)$

5. This process is repeated m times and we end up with the interferometric sum defined as

$$\underline{u}_{sum} = \sum_m \underline{u}_m(x, y, z = 0) \tag{3.4}$$

for which the total intensity is given by

$$I = \int\int |\underline{u}_{sum}|^2 \, dx \, dy. \tag{3.5}$$

By doing this process for different values of frequency we can thus find the resonant frequencies and the spectrum for the specific simulation geometry and parameters. This happens because for certain frequencies the displacement after a roundtrip acquires a phase of a multiple of 2π and so in 3.4 the individual terms are going to constructively interfere.

3.1.2. 1D–displacement approximation

Since we are interested in modes which are mainly z–polarized there are some approximations we can use to make the simulation less computationally expensive:

- we can ignore the transverse part of the displacement by setting $u_x = u_y = 0$.
- Since the polarization vectors of the two quasi–transverse slowness surfaces are mainly in the x–y plane, the mode is mainly quasi–longitudinal and so we can only consider this slowness surface.
- Finally, as described in [20] we can further simplify the simulation by performing a Taylor expansion around the $[0, 0, 1]$ direction of the slowness surface.

3.1.3. Reflections

Within the approximations described in section 3.1.2, one addition is to account for the acoustic impedance mismatch between bulk and piezoelectric materials and check how that affects the fundamental mode's linewidth and its profile.

Any propagating wave in material 1 meeting the interface with material 2 will have a part of that gets reflected and the remaining transmitted. In the case of a dome, the transmitted part will face the same interface but from the piezoelectric material side and will either be transmitted into the bulk directly or perform a number of reflections before doing so. The first three terms of this propagation are shown in Figure 3.2. The coefficients of reflection and transmission, under normal incidence, according to [19] are:

$$R_{12} = \frac{Z_1 - Z_2}{Z_2 + Z_1} \qquad \text{and} \qquad T_{12} = \frac{2Z_1}{Z_2 + Z_1}. \tag{3.6}$$

Usually in the HBAR devices only the upper part of maximum thickness t is the piezoelectric, while the remaining is bulk.

During step 4 of the BeamProp algorithm and based on equation 3.3 the displacement after propagating back and forth through the dome will thus be:

$$\begin{aligned}
u_z\prime(x,y) &= u_z(x,y) * [e^{-j2h_1(x,y)k_0} R_{12} + e^{-jh_1(x,y)k_0} T_{12} e^{-j2h_2(x,y)k_0} T_{21} e^{-jh_1(x,y)k_0} \\
&\quad + e^{-jh_1(x,y)k_0} T_{12} e^{-j2h_2(x,y)k_0} R_{21} e^{-j2h_2(x,y)k_0} T_{21} e^{-jh_1(x,y)k_0} + ...] \\
&= u_z(x,y) e^{-j2h_1(x,y)k_0} [R_{12} + T_{12} e^{-j2h_2(x,y)k_0} [1 + e^{-j2h_2(x,y)k_0} R_{21} + (e^{-j2h_2(x,y)k_0} R_{21})^2 + ...] T_{21}] \\
&= u_z(x,y) e^{-j2h_1(x,y)k_0} [R_{12} + T_{12} e^{-j2h_2(x,y)k_0} T_{21} \sum_{k=0}^{\infty} (e^{-j2h_2(x,y)k_0} R_{21})^k] \\
&= u_z(x,y) e^{-j2h_1(x,y)k_0} [R_{12} + \frac{T_{12} e^{-j2h_2(x,y)k_0} T_{21}}{1 - e^{-j2h_2(x,y)k_0} R_{21}}],
\end{aligned} \tag{3.7}$$

with $h_1(x, y)$ and $h_2(x, y)$ the height distributions for the bulk and piezoelectric parts of the dome accordingly.

BeamProp3D implementation

In the previous subsubsection only displacements in the z–direction were assumed. However even the polarization vectors of the quasi–longitudinal slowness surface are not only

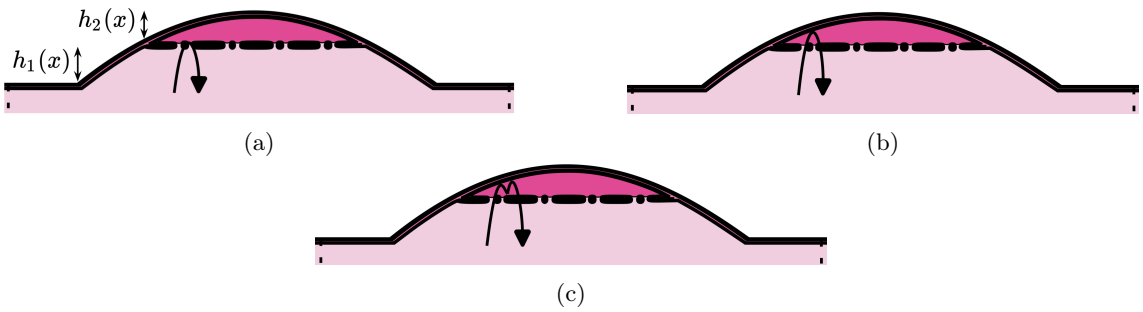

Figure 3.2: Three of the possible cases for sound wave propagation at the interface of two materials in the dome of an HBAR. (a) Reflected at interface. In addition, we show which heights $h_1(x)$ and $h_2(x)$ correspond to. (b) Transmitted from bulk to piezoelectric and from piezoelectric to bulk. (c) Transmitted from bulk to piezoelectric, reflected at interface once, and then transmitted to bulk.

z–polarized, even though that is the dominant direction. Including u_x and u_y would:

(a) allow us to identify also transverse modes

(b) let us study losses due to polarization conversion.

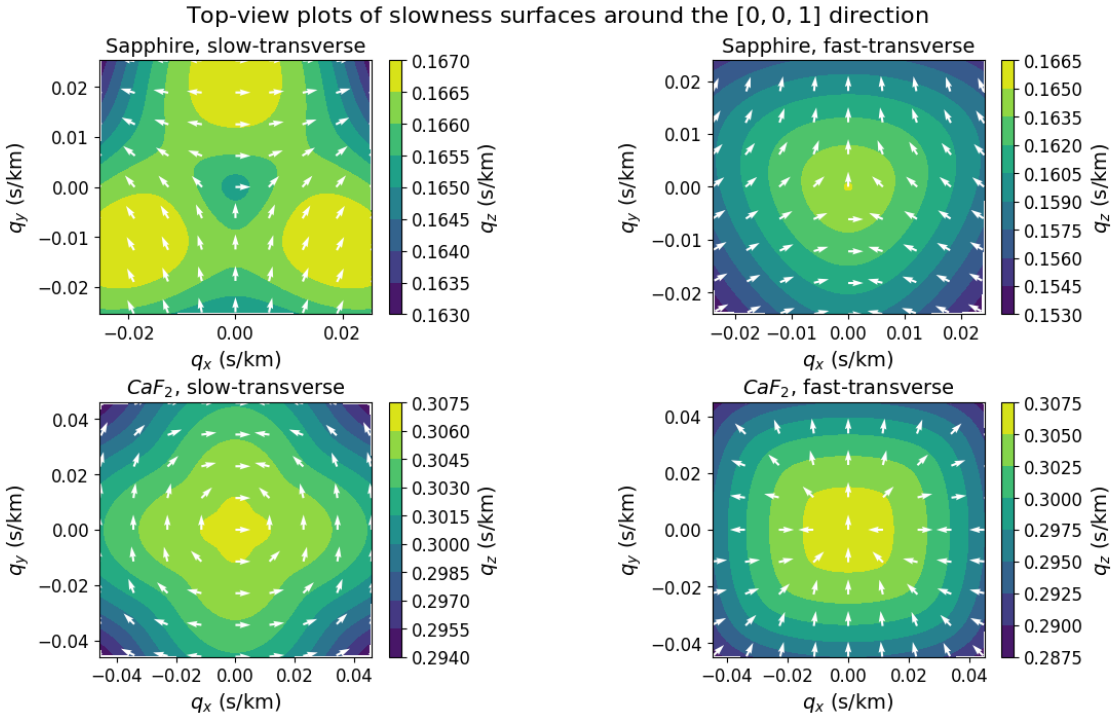

Figure 3.3: Contour plots of the quasi–transverse slowness surfaces for sapphire and CaF_2. The arrows on the plots represent the x– and y–components of the polarization vectors.

This new tool gives the option of introducing an initial displacement that is not just z–polarized. As a result, if we choose an initial Gaussian intensity profile in all three directions, meaning $u_{x,init} = u_{y,init} = u_{z,init}$ then what we expect is to be able to find quasi–transverse modes along with the quasi–longitudinal ones. If we look at equation 3.5, we can decompose it into

$$\begin{aligned} I &= \int\int |\underline{u}_{sum}|^2 \, dx\, dy = \int\int |\sqrt{u_x^2 + u_y^2 + u_z^2}|^2 \, dx\, dy \\ &= \int\int u_x^2 \, dx\, dy + \int\int u_y^2 \, dx\, dy + \int\int u_z^2 \, dx\, dy = I(u_x) + I(u_y) + I(u_z). \end{aligned} \tag{3.8}$$

The quasi–transverse modes will be shear waves and so will become apparent by plotting the intensity spectrum of $I(u_x) + I(u_y)$, while the quasi–longitudinal modes will cause peaks in $I(u_z)$.

In Figure 3.4 we see, for the same geometry, in terms of substrate length, dome shape and dimensions and piezoelectric thickness, what these simulated spectra look like for the case of sapphire (the one actually used in the devices we measured) and CaF_2 as the bulk material. In both cases the frequency spectrum is more than one –longitudinal mode– FSR, which is clear from having two collections of peaks in $I(u_z)$ separated by a low intensity region. On the right plot we also see four mode families in the plot of $I(u_x) + I(u_y)$, indicating the shear modes. The FSR difference of these modes, compared to the longitudinal ones, is expected since for CaF_2 the phase velocities in the $[0, 0, 1]$ direction are $[u_{ph}^{t_1}, u_{ph}^{t_2}, u_{ph}^{l}] = [3.2655, 3.2655, 7.2044]$(km/s) and $FSR = u_{ph}/2L$. The exact same behaviour is expected for sapphire, for which

$$[u_{ph}^{t_1}, u_{ph}^{t_2}, u_{ph}^{l}] = [6.0567, 6.0567, 11.1972](\text{km/s}), \tag{3.9}$$

according to the values in *Appendix* B. However this is not the case. There seems to be

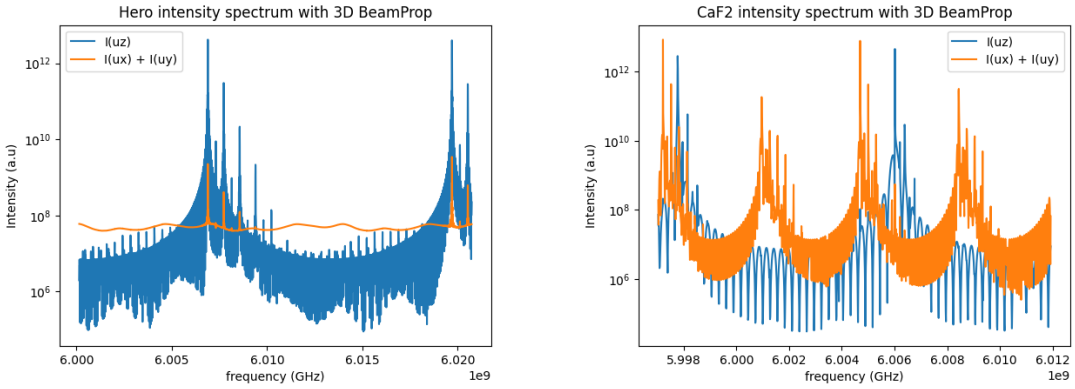

Figure 3.4: Spectra from 3D BeamProp simulation for geometry of a sample with the actual sapphire bulk material and with CaF_2. As *hero* we refer to a particular device in the group, which has a great performance in terms of strong coupling.

a quasi–constant transverse intensity level. There are two indications that there should be transverse modes: one is that experimentally we see modes repeating at this expected FSR, which is also reported in another work[21], and also in COMSOL we can see modes polarized in the x–y plane.

Unfortunately this issue has not been solved by the end of this thesis. The origin however seems to have been identified. Going back to Figure 3.3, we observe that the slowest surface of sapphire has a different form from the other surfaces. Indeed this surfaces does not have a parabolic shape with the highest value on–top, but rather a dip at the center. What that would mean, from solid mechanics, is that energy would be focused in that direction. This effect is called *phonon focusing* in literature.

It is not clear if that is the reason behind this transverse intensity or whether (quite likely) there is some mistake in the code or the values leading to this behaviour. In order however to isolate the behaviour of the two quasi–transverse surfaces, the approximated (1D) version of BeamProp was used. Of course usually this means only considering u_z and the values of the quasi–longitudinal slowness surface, but one can just import the values of any other surface and treat the simulation as if the one used is the quasi–longitudinal one. When running the approximated version only considering the fast–transverse surface, then the spectrum looks as expected, a series of collections of peaks after each FSR, indicating the usual fundamental and higher–order modes. However, when running the

same simulation using the slow–transverse values then there were no resonant peaks, as seen in Figure 3.5.

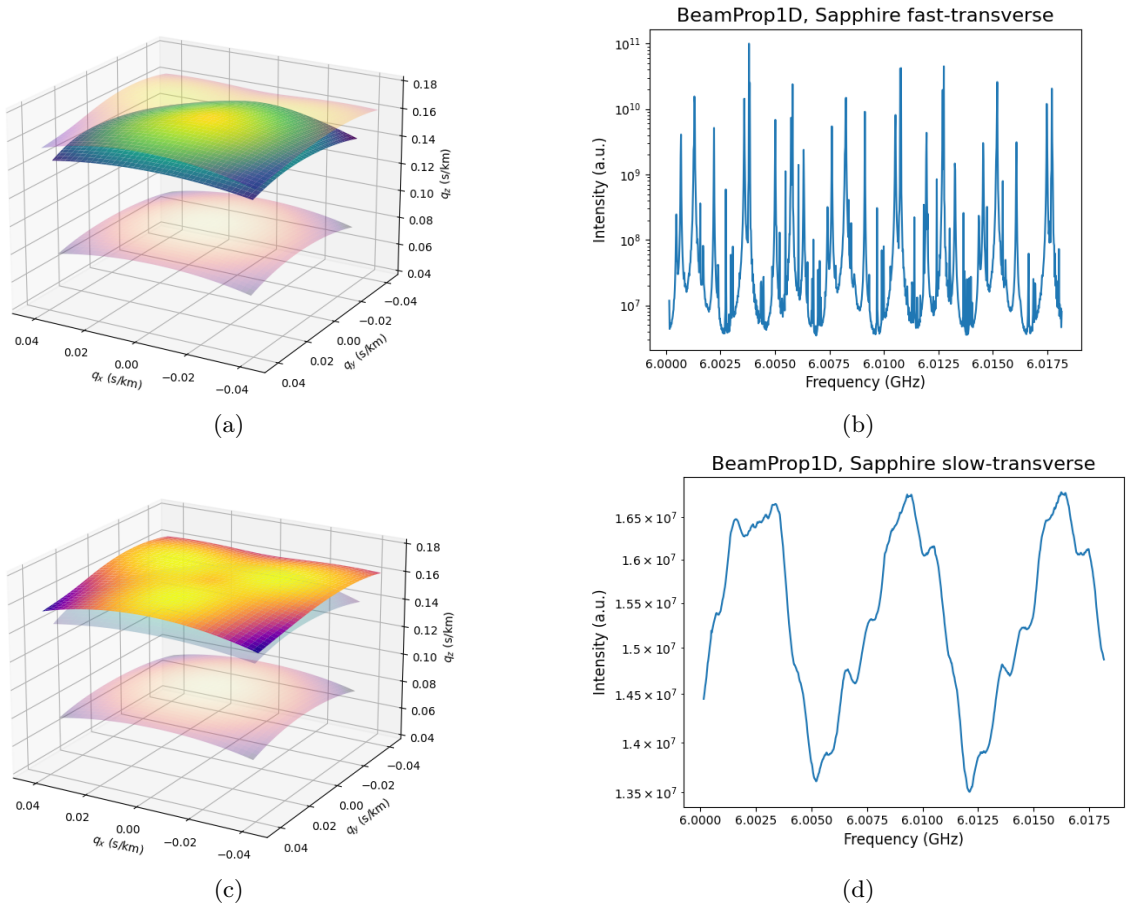

Figure 3.5: One the left are the slowness surfaces used to create the intensity spectra on the right, using BeamProp1D. (a) Fast–transverse slowness surface of sapphire. (b) Spectrum using fast–transverse slowness surface of sapphire. (c) Slow–transverse slowness surface of sapphire. (d) Spectrum using slow–transverse slowness surface of sapphire.

It remains an open question is why in the 3D version we do not see both the mode spectrum of the fast-transverse and the slow-transverse slowness surfaces, but the effect of the slowest surface "takes over". As stated in the BeamProp algorithm section, with more information found in Appendix A, for a particular $[q_x, q_y]$ pair the polarization vectors of the three surfaces are not orthogonal, because they do not correspond to the same direction. We have a grid of points for each of which three non–orthogonal vectors are assigned. If for each point we look at the dot product of these vectors it is less than 10^{-3}. So one might expect that if a mode of the fast–transverse surface is excited it will not be affected as much by the slow–transverse. On the other hand both surfaces have mainly x– and mainly y–polarized eigenvectors. As a result any u_x and u_y excitation is going to involve both and in a sense "entangle" them.

3.1.4. Resonant Mode Linewidth

We want to study how the linewidth of a resonant mode evolves with the number of roundtrips performed. Let us consider a cavity of length L, a resonant frequency $f_0 = mv_{ph}/2L$ with $m \in \mathbb{N}$ and a plane wave with wavenumber $k_z = 2\pi f_0/v_{ph}$. The intensity

after N roundtrips, similarly to the equation 3.5 will be:

$$I(f_0) = |\sum_{n=0}^{N} u_n|^2 = |\sum_{n=0}^{N} u_0 e^{ik_z n 2L}|^2 = |\sum_{n=0}^{N} u_0 \underbrace{e^{i2\pi mn}}_{1^n}|^2 = (N+1)^2 u_0^2 \tag{3.10}$$

Since the metric for losses is the Full–Width at Half–Maximum (FWHM), let us see how the frequency $f = f_0 + \delta$ for which $I(f) = I(f_0)/2$ is related to N. We have:

$$\begin{aligned}
I(f) &= |\sum_{n=0}^{N} u_0 e^{i2\pi mn} e^{i2\pi 2Ln\delta/v_{ph}}|^2 \\
&= u_0^2 |\sum_{n=0}^{N} e^{i2\pi 2Ln\delta/v_{ph}}|^2, \qquad x \coloneqq 2\pi 2L\delta/v_{ph} \\
&= u_0^2 |\sum_{n=0}^{N} e^{ixn}|^2 \\
&= u_0^2 |\frac{e^{ix(N+1)} - 1}{e^{ix} - 1}|^2 \\
&\approx u_0^2 |\frac{e^{ix(N+1)} - 1}{ix}|^2, \qquad x = 2\pi m\delta/f_0 \ll 1 \text{ since } \delta \sim \text{kHz} \\
&= \frac{u_0^2}{x^2} |e^{ix(N+1)} - 1|^2.
\end{aligned} \tag{3.11}$$

In order to get a sense of how δ scales with N we also assume $(N+1)x \ll 1$ so that we expand the remaining exponential, even though this approximation is not valid. By keeping the first four terms we get:

$$\begin{aligned}
\frac{1}{2} u_0^2 (N+1)^2 &= \frac{u_0^2}{x^2} |ix(N+1) - \frac{1}{2}[x(N+1)]^2 - \frac{i}{6}[x(N+1)]^3|^2 \\
1 &= 2|i - \frac{1}{2}[x(N+1)] - \frac{i}{6}[x(N+1)]^2|^2 \\
1 &= 2[(1 - \frac{1}{6}(N+1)^2 x^2)^2 + \frac{1}{4}(N+1)^2 x^2] \\
x^2 &= \frac{-3 \pm i\sqrt{63}}{2(N+1)^2} \\
x^2 &\propto \frac{1}{(N+1)^2} \\
\delta &\propto \frac{1}{N+1}.
\end{aligned} \tag{3.12}$$

From the above, we may expect the linewidths we find from BeamProp to be inversely related to N, up to the point where the phase difference accrued between two waves of different frequency is no longer limited by the propagated length but other factors, i.e. losses.

3.2. Coupling Rates – COMSOL

There are three methods which have been used thus far to estimate the electromechanical coupling rates between a microwave resonator and an HBAR. One is to use the electric field values obtained from finite element simulations performed in the *Ansys* software package and the phononic mode profiles from BeamProp. However due to the BeamProp3D issues described above this would only allow us to look into longitudinal modes, since we do not get

transverse modes, and hence their profiles, so we cannot use it in combination with Ansys. The other two are both in COMSOL Multiphysics and are based on work done previously in the group and described in [22]. In this work they integrated in the same COMSOL simulation the so called $\hbar BAR$, meaning the substrate with the superconducting qubit and on top of it the substrate with the piezoelectric material that contains the mechanical modes. This gives the capability of performing a single simulation to find the behaviour of the system, meaning predicting the frequencies, coupling rates and so on. One option is to perform a coupled simulation using both the

- *Electromagnetic Waves, Frequency Domain (emw)* and the
- *Structural Mechanics*

physics interfaces and the other to do these simulations separately and use equation 2.30 or some other formula in the post–processing step to get the result.

For our case the latter option for calculating the coupling rates was used, the reason being that it is computationally much less expensive and sufficient for our study. A great advantage of using this approach is that within a single file the volume integration can be done with a more realistic spatial distribution of the electric field. This would be even more useful if the modes of interest had more complex profiles.

An important aspect of these simulations is how to implement the correct material's crystal orientation in the case of Lithium Niobate in COMSOL. For this we can use the method discribed in [i] by which the steps are:

1. in the **Definitions** subnode under the **Component** define a **Rotated Coordinate System**. The new system is generated from the "global" one by performing three rotations by the Z, then the X and then the Z axis again. These rotations are sufficient for the new system to have any direction. In order for the Y axis to be rotated to the z–direction we only need to perform a 90° rotation about X, so the angles for rotation are $[0, 90°, 0]$.

2. For the mechanical properties of the material we can either create a **Piezoelectric Material** or an additional **Linear Elastic Material** subnode of **Solid Mechanics** in which we simply choose the new, rotated coordinate system and the material properties will be adjusted.

3. In case we were working with the **Electrostatics** physics interface of COMSOL then in the previous step we would set the **Piezoelectric Material** and this would be sufficient. However we are using the emw interface and due to the lack of a direct Multiphysics–Coupled interface we need to also rotate the coordinate system at the subnode of the modified relative susceptibility, again as defined in [22]. Note however that this needs to be done at the level of the Wave Equation subnode and not by an effective medium.

4. Finally, another distinction from the original work in [22] is that in the post–processing step, when working with the **Results** of the simulations we need to pay attention in using the material properties as defined in the global coordinate system. For example, for the $(1, 1)$ element of the coupling matrix in the rotated coordinate system, instead of *solid.eES11* which we would normally use, we need to use *solid.eESgX1*, which couples an E-field in the x direction of the global coordinate system to a longitudinal S_{xx} strain field. .

5. To verify that these steps actually lead to the desired changes we go to **Results** →**Datasets** →**Cut Point 3D** where we define a random point within the piezoelectric volume. After that we go to **Derived values** →**Point Evaluation****Point Matrix Evaluation** and evaluate some material property.

[i] https://www.comsol.com/blogs/piezoelectric-materials-applying-the-standards/

Chapter 4

Simulation Results

As described in the previous chapter, in cQAD a fundamental condition for performing useful operations for quantum information processing, and more, is that the coupling rate g exceeds the system losses, i.e. the mechanical dissipation rate κ_m and the qubit loss rate γ_q. This work does not contain a study on the qubit, but on the other two metrics in two sections.

The first section is dedicated to the mechanical dissipation rate κ_m and mainly on work done using BeamProp and consists of two parts. First, within the 1D approximation described in the previous chapter, we investigate if diffraction losses are the limiting factor of our samples and if this is modelled properly only when considering reflections. Furthermore, we look into the effect of radius of curvature on diffraction losses to find if shaping the dome of our samples in a different manner would lead to better lifetimes and the limit at which they decrease. Then the second part is a study using BeamProp3D, where propagation back and forth inside the dome leads to redistribution of plane–wave decomposition and now diffraction losses come from all slowness surfaces.

The second section is based on work done previously in the group and used to simulate the coupling rate of the devices in case of Lithium Niobate. More specifically we estimate the coupling rate of an upcoming sample. In order to verify the method used we also calculate the coupling rate for a sample that has been measured in the lab. Finally, we look into increasing the coupling rate by taking advantage of the piezoelectric properties of Lithium Niobate as in B.6 and coupling to shear modes instead of longitudinal.

4.1. Phonon Lifetime

4.1.1. BeamProp1D – Reflections

The loss mechanism that we include in BeamProp is decay through diffraction. Choosing the shape of the HBAR device as a plano–convex cavity, similarly to the case of electromagnetic cavities, happens in order to contain the mode. As the beam propagates, it expands and diverges. In a plano–plano cavity this diffraction would cause energy to get lost as radiation into the bulk, but having a dome–shape provides stability. So the implementation of this energy loss is done with the calculations of $u_z\prime(x, y, z = 0)$ and $u_z\prime(x, y, z = L)$, by multiplying the displacement values of the points that "live" outside the under–dome region with a number, β, smaller than one as seen in Figure 4.1. The further away from that region the more is that point "penalized".

The interface of the bulk and piezoelectric materials acts as a partially reflective flat surface and so beams that are not propagating exactly normal to that interface will be driven away from the under–dome region. As seen in equations 3.6 the reflection (transmission) coefficient becomes larger (smaller) with higher acoustic impedance mismatch. This is the case when combining Sapphire with Lithium Niobate compared to Aluminum Nitride and led to the idea behind accounting for reflections.

When running the simulation we define the specific *number of roundtrips* for which the displacement is going to propagate in the device. As a result, as seen in equation 3.12, by increasing the number of roundtrips the FWHM should keep decreasing. If, however, diffraction losses are sufficient, then the additional terms added to the total displacement

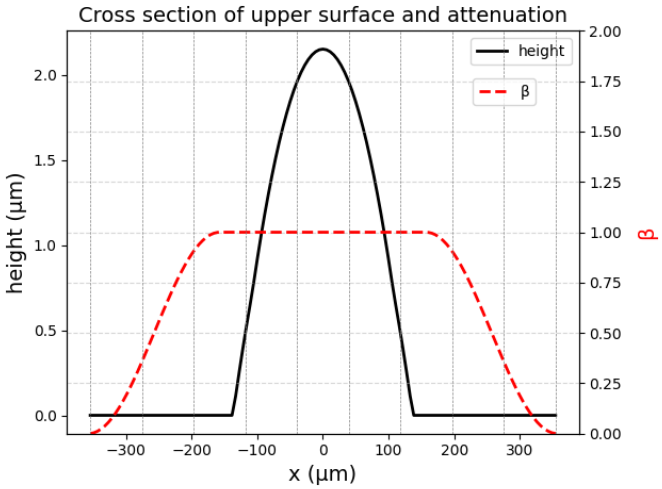

Figure 4.1: Cross section of the upper surface of the HBAR, flat part and dome, along with the profile of β, the number that multiplies the displacement to introduce attenuation. Decay starts from $20\mu m$ outside the edge of the dome.

Label	Bulk length (μm)	Dome max height (nm)	Piezoelectric material	Piezo max thickness (nm)	Dome RoC (mm)
Hero	435	1878	AlN	1156	35
Old LN	665	1360	$LiNbO_3$	690	45.6
New LN 1	230	1440	$LiNbO_3$	667	7.41
New LN 2	230	1440	$LiNbO_3$	667	3.3

Table 4.1.: Information regarding geometric and materials for four samples. The first two have been measured, while the last two have been fabricated, but not yet bonded to qubits and measured. For the *Hero* sample lifetimes and coupling rates can be found in [23], while for *Old LN* in Table 5.1.

(equation 3.4) will become insignificant and the FWHM will converge to a higher number than in the lossless case. If diffraction losses are the main decay factor then we expect that this number will approach the one of the actual devices.

The sufficient number of roundtrips depends on the specific device characteristics, like the sound velocity in the bulk material or its length. From the second to last row of equation 3.12 and with the definition of variable $x \coloneqq 2\pi 2L\delta/v_{ph}$ in mind, if we also consider the length of the HBAR as a variable then $\delta \propto 1/(N+1)L$. This means that the shorter the HBAR, the number of roundtrips needs to be higher for sufficient linewidth decrease.

The results of this study are shown in Figure 4.2 where we see the linewidth convergence for the four samples described in table 4.1 with both implementations, with and without accounting for reflections. Samples *Hero* and *Old LN* are the two devices that have actually been measured, with the former having lower phonon decay rate of $\sim 2\,$kHz and being the device that papers [23][24][25][26] are based on. We see that no matter which approach was used, all samples seem to not be diffraction–limited via BeamProp1D as their linewidth converges to values much lower than the experimental.

Even though the samples are not diffraction–limited according to our study, there might also be a way to improve their ideal performance. For this reason we look at the effect of radius of curvature (RoC) on the phonon lifetime. More specifically we calculate the FWHM of samples that have the same geometric and material characteristics as the *Hero* device other than the RoC. It is sufficient to restrict the number of roundtrips, for computational reasons, to 25.000 because significant improvements (lower FWHM) or deterioration (higher FWHM) would become apparent even from this stage. This number was chosen

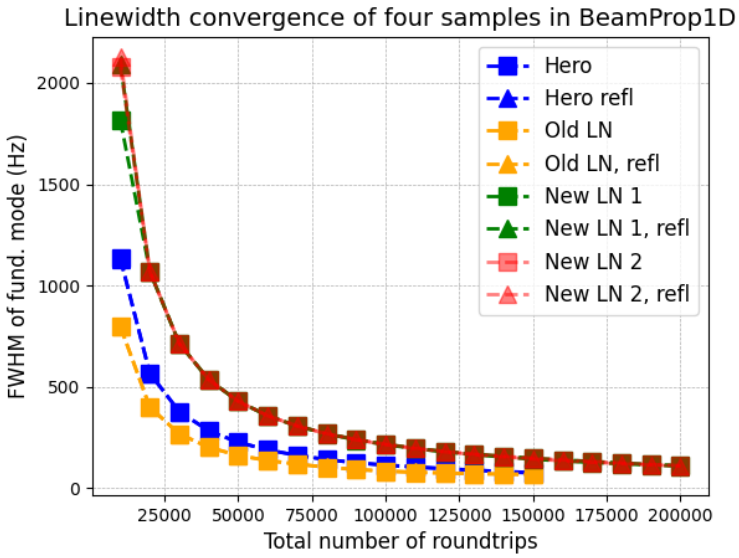

Figure 4.2: Convergence plot the fundamental mode of the four samples in table 4.1. In all cases the mode frequency is close to 6 GHz.

because for the *Hero* sample the calculated FWHM is about 500 Hz, close to the experimental case. A verification however that the samples' FWHM evolves as expected was done for two samples near the opposite sides of the RoC spectrum with both methods and their results are shown in Figure 4.3. Looking at the log–log plots, linewidth initially has the $1/N$ dependence derived in the previous chapter, but this changes above 140.000 roundtrips.

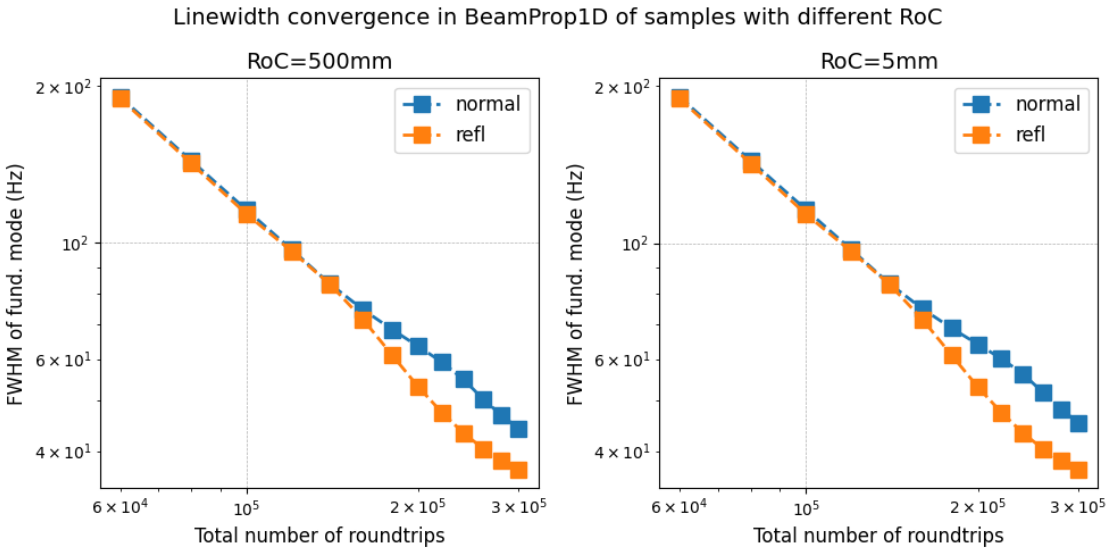

Figure 4.3: Evolution of FWHM for the fundamental mode for two different radii of curvature. The remaining parameters for both simulations are the ones for the *Hero* sample in Table 4.1.

The results of the study relating linewidth to radius of curvature are shown in Figure 4.4(a). We see that in the range from about 2 mm and up to 500 mm RoC there are not significant changes to the FWHM of the simulated samples. We also observe that stability will fail for about 1 mm when we consider reflections and for 0.5 mm with the original, "normal", code. A minimum requirement for a working cavity is that it satisfies the cavity stability criterion [12][27]. This leads to an absolute lower limit on the radii of curvature

of the dome for a particular choice of materials and chip thickness and approaching this lower limit will lead to a steep increase in cavity losses. As a result the specific radii that led to instability here are not universal.

We also wanted to study the effect of accounting for reflections to the width of the fundamental mode. This is important for the design of the superconducting qubits, as we want the shape of their electric field to match the phononic mode. As seen in Figure 4.4(b) this implementation leads to reduction in mode width. This is again not a universal result however. There were other cases where the reflection code led to wider mode profile, which makes it more difficult to interpret this behaviour.

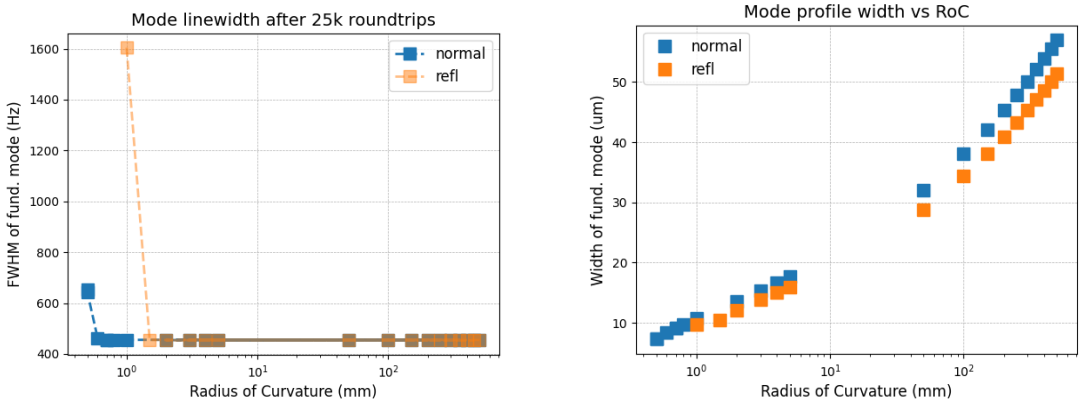

(a) (b)

Figure 4.4: Study of how RoC affects the losses of the fundamental modes and their profiles for devices with geometry similar to that of *Hero*. (a) Effect of radius of curvature on mode FWHM. (b) Effect of radius of curvature on mode profile.

As a final note here let us mention that there was an attempt to verify BeamProp1D through COMSOL. For that, the same geometry was created in both programs: 50 µm sapphire bulk, circular dome of varying RoC and thickness 1156 nm, whole dome consisting of *AlN*. In order for the comparison to make sense we used the *Prescribed Displacement* option in COMSOL to only consider u_z. In COMSOL, once the user finds the eigenmodes there is a *Q-factor* calculation in the post–processing part. The idea was thus to make a series of simulations, going to smaller RoC and find for which one each method fails, similarly to what was done in Figure 4.4(a). The issue that we came across though was that in COMSOL we expect Q to converge at some point as the meshing becomes more detailed. This however was not achieved within our RAM limitations, meaning the more detailed the mesh the larger the Q, without converging. So the above study has not been verified via COMSOL.

4.1.2. BeamProp3D

Even though the issue described in section 3.1.3 has not been solved, the same convergence study of the four samples of table 4.1 was done with BeamProp3D and the results are shown in Figure 4.5. For the *Hero* and *Old LN* samples the simulations show again that they are not diffraction–limited. However, the upcoming *New LN 1* and *New LN 2* are. Since for these we have already surpassed the RoC for which the cavity becomes lossy, the smaller the RoC the more the losses, and so *New LN 2* converges faster than *New LN 1*. It will thus be very interesting to see what the experimental lifetimes will be once those samples are actually measured. Furthermore, additional investigation needs to be done to explain this, similarly to the 1D case and the 1D case including reflections, like a study of linewidth with radius of curvature. The reason why this has not been done is again the unsolved issue for the case of sapphire.

The issues of BeamProp3D make us question the simulation results. One possibility to benchmark these simulations is through COMSOL, which has been prevented due to hardware limitations thus far, since solving for displacements in all directions would increase the simulations degrees of freedom compared to when we were using the *Prescribed Displacement*. As a result we would definitely not be able to reach a Q convergence. An approach to overcome this would be to perform simulations for smaller bulk sizes and/or using a more powerful PC.

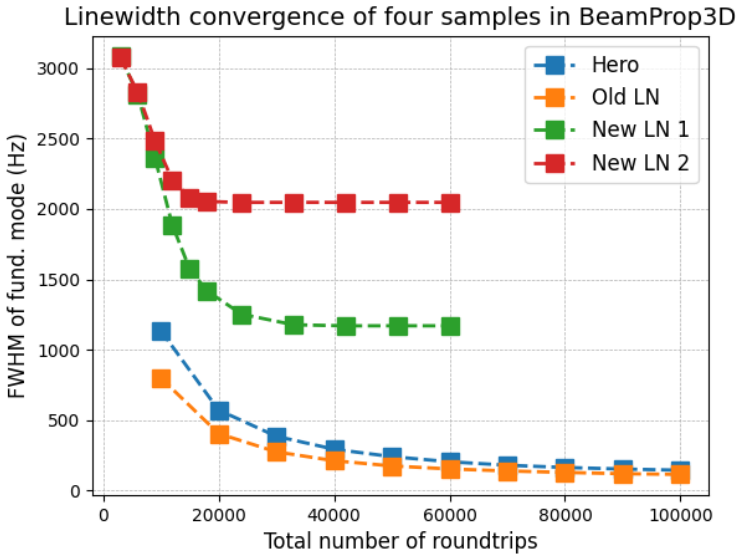

Figure 4.5: Convergence plot the fundamental mode of the four samples in table 4.1.

4.2. Coupling Rate

With all the specifics described in section 3.2 in mind, the coupling rates for the upcoming *New LN 1* sample are shown in Figure 4.6. In the post–processing step we look into the flat side of the HBAR to find the mode profiles, which correspond to the Hermite–Gaussian (HG_{ij}) modes shown in Figure 4.7. In general through the *Structural Mechanics* eigen–mode solution one can find many higher order modes, but the higher the order (meaning higher values for i, j) the lower the coupling rate, compared to the fundamental mode. This is due to the fact that we are integrating in a volume where we will have positive and negative regions of displacement. Figure 4.6 therefore only includes longitudinal modes up to order 3, meaning with indices HG_{ij} such that $i + j \leq 3$, and the two fundamental (HG-00) transverse modes that are x– and y–polarized.

An important note is that these values are acquired for a bulk length of 40 µm to make the simulation less computationally expensive. In order to predict the values for the upcoming sample, g_{sim}, since $g \propto 1/\sqrt{V}$ [22], where V is the volume of the mechanical mode, we scale the values obtained from COMSOL, g_{COMSOL}, by the difference in simulated and actual mode volume as:

$$\frac{g_{sim}}{g_{COMSOL}} \approx \frac{1/\sqrt{V_{actual}}}{1/\sqrt{V_{COMSOL}}} = \frac{\sqrt{V_{COMSOL}}}{\sqrt{V_{actual}}} \approx \sqrt{\frac{L_{COMSOL}}{L_{actual}}} = 0.417. \tag{4.1}$$

Note that this scaling method ignores the change of mode width with crystal length, which is given as $w \propto L^{1/4}$. For the *Old LN* sample the simulated and experimental coupling rates are:

$$|g_{sim}|/2\pi \approx 170\,\text{kHz} \qquad \text{and} \qquad |g_{exp}|/2\pi \approx 159\,\text{kHz}. \tag{4.2}$$

From Figure 4.6 we observe the following:

- From the longitudinal modes, the only modes that are at the same order of magnitude with HG–00 are the HG–02 and HG–20. These are the first higher–order modes that have displacement at the center of the mode profile (see Fig. 4.7).
- The first shear mode shown is at 5.0637 GHz and it has the profile of a fundamental mode (HG–00) if we look at u_x and HG–10 if we look at u_z. The coupling for this is much smaller than for the fundamental longitudinal mode, but this one couples through the x–component of the electric field, not the z–component and it comes from the value of 2.37 $\mathrm{C/m^2}$ of the coupling matrix in Appendix B. Figure 4.8 shows the amplitude of the electric field components on the x–z plane inside the dome.
- The other transverse mode shown at 5.0779 GHz is the fundamental mode with y–polarization. The coupling for this is lower than for the HG-02 and HG-20, but higher than the higher order longitudinal modes. It comes from the z–component of the electric field, but has major contributions from both S_3 and S_4 (S_{zz} and S_{yz} in Voigt notation respectively), so utilizing also the 3.83 $\mathrm{C/m^2}$ component of the coupling matrix in Appendix B.

Since for sapphire, as seen in equation 3.9, the transverse phase velocity is about half of the longitudinal one, the corresponding wavelength is going to be about half as well, if we are looking at modes that are close in frequency. The piezoelectric thickness is designed to be approximately half the wavelength of the mode we want to couple to, in order to maximize the coupling rate. The above is shown in Figures 4.9 and 4.10. Figure 4.9 shows the profiles of the S_3 (for mode HG–00) and the S_4 (for mode HG-00-y at 5.0779 GHz) strain vector component on the x–z plane at the center of the piezoelectric region. Figure 4.10 shows the displacements u_z (for mode HG–00) and u_y (for mode HG-00-y) across the symmetry axis, z, of our geometry. Both show that the fundamental longitudinal mode has approximately half a wavelength of displacement (or strain) inside the piezoelectric region, while the shear modes fit roughly a full wavelength inside this region.

So then a question that naturally arises is whether the largest component of the piezoelectric's coupling matrix can be used as an advantage instead of a drawback. For this to happen we need to couple the strongest to the component S_4 of the strain vector in Voigt notation, instead of the S_3 we use now. For this we did a simulation with a device that has the same geometric characteristics as the above (bulk length, dome RoC, materials), but half the piezoelectric thickness/dome height, so as to maximize the coupling to the shear modes instead of the longitudinal modes.. The results for that are shown in Figure 4.11. We see that in this configuration we can achieve higher coupling rates, from 270 kHz that we had before to about 400 kHz. The drawback is that the coupling to the unwanted/higher–order modes will also be higher.

We note that the estimations heavily depend on the material properties used for the simulations. But in reality we do not have the exact values of properties like the piezoelectric tensor or the refractive index of our sample. This issue is mentioned for example in [21], for the value of a component of the coupling matrix of Aluminum Nitride. Furthermore, we do not know how these values change in milliKelvin temperatures. But even though the absolute values might diverge, the relative coupling rates should hold.

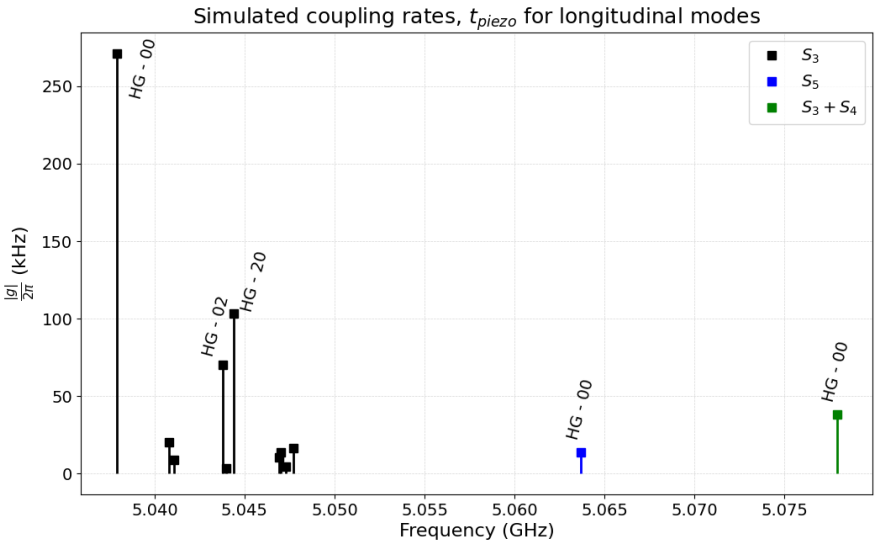

Figure 4.6: Coupling rates for the upcoming *New LN 1* sample, with piezoelectric thickness 667 nm.

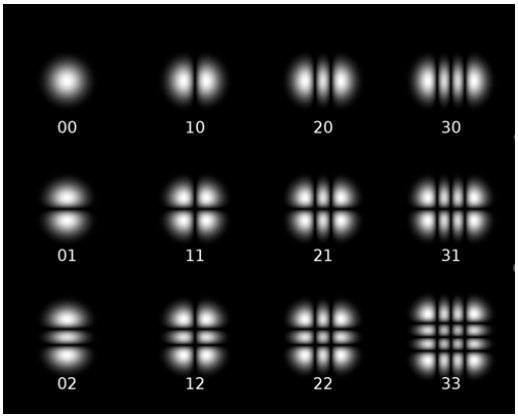

Figure 4.7: Hermite-Gaussian mode profiles. Image from [28].

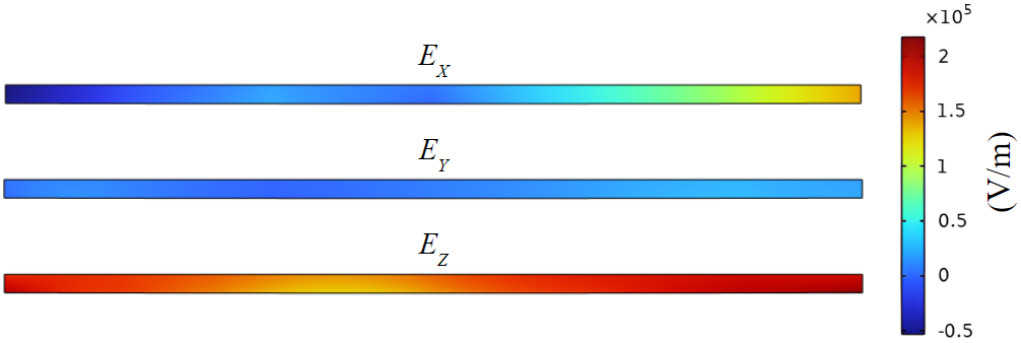

Figure 4.8: Electric field components on the x–z plane inside the dome. The colourbar is common for all components, its lowest (highest) value is the minimum (maximum) E–field value of the plotted data. The region shown above has length ≈ 31 µm and height 667 nm.

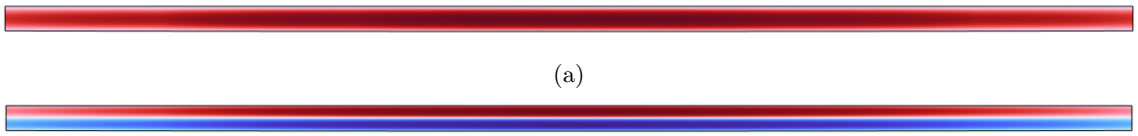

(a)

(b)

Figure 4.9: (a) Profile of the fundamental S_3 mode on the x–z plane inside the dome region, the first mode in Figure 4.6. (b) Profile of S_4 mode on the x–z plane inside the dome region, the last mode in Figure 4.6. The color–scale is symmetric, with white corresponding to zero, red to positive and blue to negative. The particular piezoelectric thickness of 667 nm is thus optimized for coupling strongly to longitudinal modes. The region shown above has length $\approx 31\,\mu$m and height 667 nm.

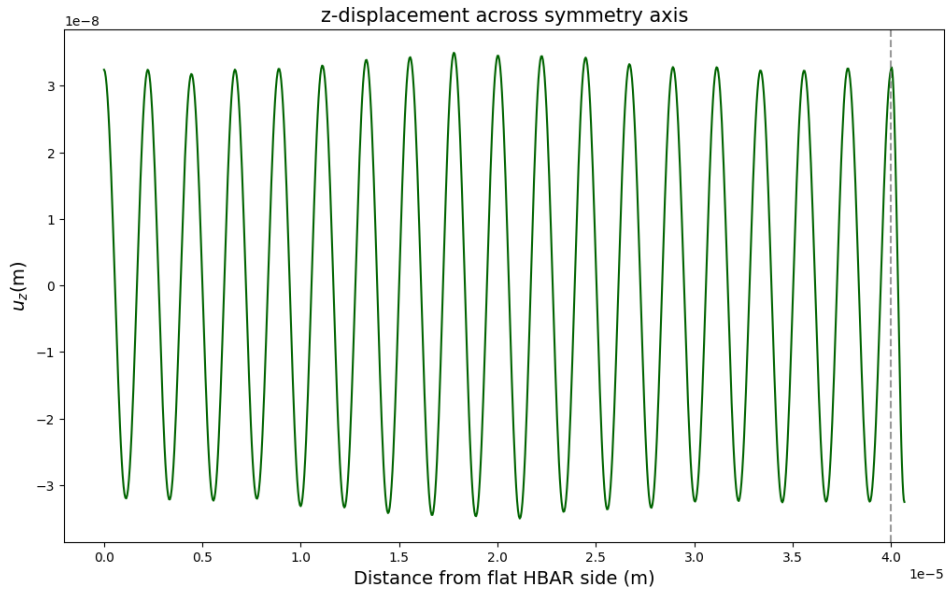

(a)

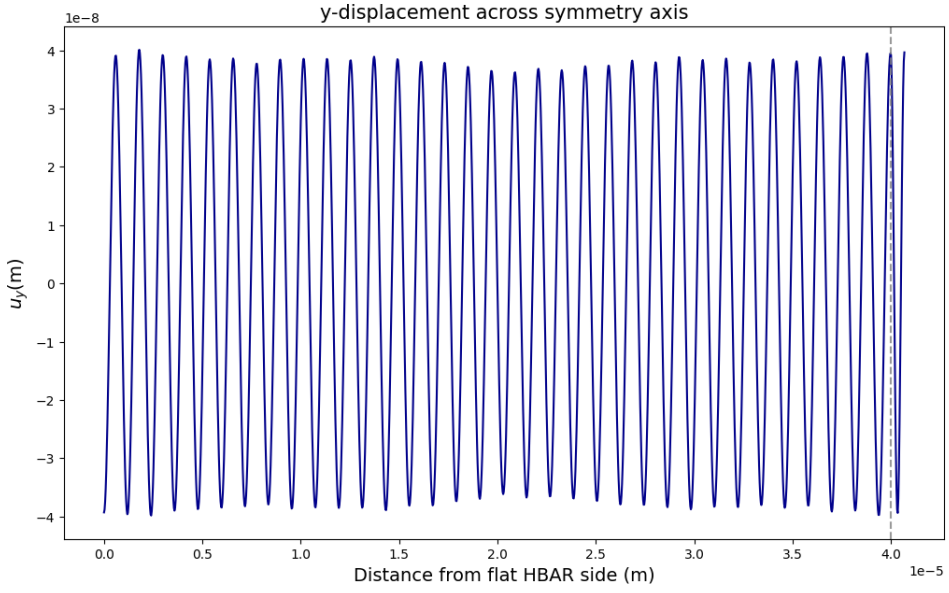

(b)

Figure 4.10: Displacement components of the same modes from Figure 4.9. Both plots show the displacements for the fundamental modes across a line that starts from the flat surface of the bulk until the top of the dome for $x = y = 0$. The dashed line indicates where the dome, and thus the piezoelectric material starts. The part left of the dashed line is the displacement along the z–axis of the fundamental modes in sapphire and the part right from the dashed line in Lithium Niobate. (a) Longitudinal fundamental mode, the first mode in Figure 4.6. (b) Shear fundamental mode, the last mode in Figure 4.6.

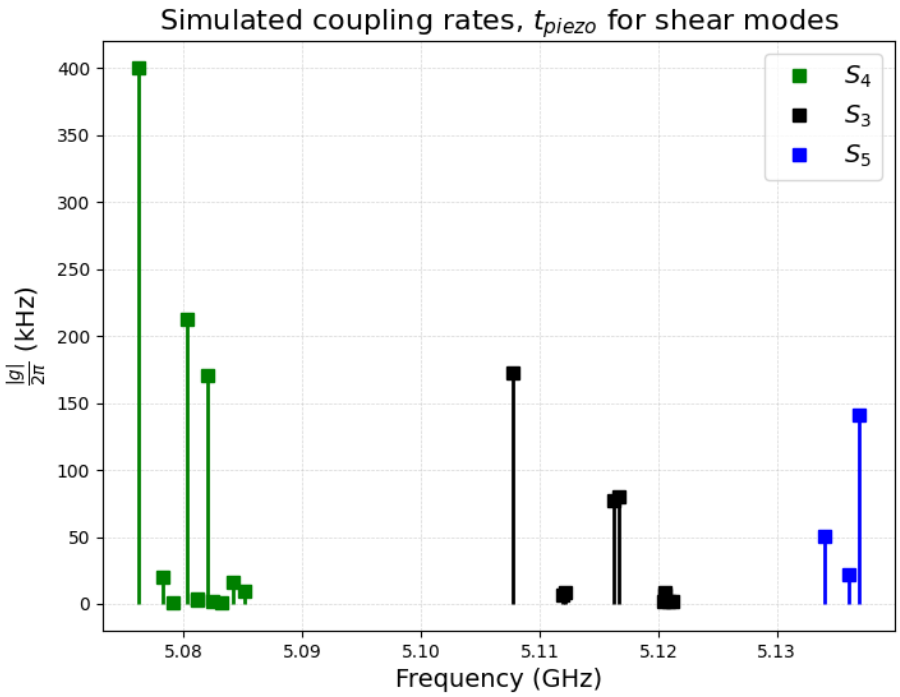

Figure 4.11: Coupling rates for a device with the characteristics of the upcoming *New LN 1* sample, but with half the piezoelectric thickness, 333.5 nm.

4.3. Conclusions

In this chapter we saw that:

- with BeamProp1D the samples that have been measured along with the upcoming ones are not limited by diffraction losses.
- With BeamProp3D, which includes diffraction originating from polarization conversion, the measured samples have again not been limited, but the upcoming ones will be if their experimental phonon linewidths approach 2 kHz.
- The *New LN 1* sample is expected to have coupling rate to the fundamental longitudinal mode of about 270 kHz.
- If the same substrate is fabricated such that it has a piezoelectric thickness of 333.5 nm then it will couple to the fundamental shear mode with rate of about 400 kHz.

Chapter 5

Experimental results

This chapter contains three sections. The first is dedicated to the description of the experimental setup with an emphasis on the way the measurements are performed. In the second section we find some characteristics of the Lithium Niobate devices that have been measured in the lab and their results are presented in the third section.

5.1. Setup and measurement sequence

The experiment consists of a typical Circuit Quantum Electrodynamics setup[2] with the addition of the flip–chip bonded substrate with the piezoelectric dome for the phonon modes. The two substrates, shown in Figure 5.1(b) are placed in a microwave cavity, which is placed in a dilution refrigerator at a few milliKelvin. Excitation and readout pulses are sent through the input line to one of the connectors of the microwave cavity. The collected signal from the other connector passes through the output line and is used to get information about the system. This corresponds to a microwave cavity transmission measurement.

Once the cooldown is done there are a few steps that need to be done before the HBAR characterization:

- initially there is a frequency scan of the readout signal in order to identify the frequency of the cavity, which usually is around 8 GHz. In this case we are far detuned from the qubit transition, which remains in the ground state. The readout pulse is optimized, in terms of amplitude and duration, and set for the remainder of the experiment.

- Then we scan the frequency of another pulse to find the qubit's frequency while monitoring the transmission of the readout pulse. This is known as *two–tone* spectroscopy[29]. While the qubit is not excited the readout signal is at a constant level. When the qubit gets excited then the spectrum is going to have a dip at that frequency. This is because the frequency of the cavity will be shifted due to dispersive interaction with the qubit's state[2]. If the excitation pulse is long then the qubit's state will be constantly making rotations around the Bloch sphere and so on average it will be on an equal mixture of ground and excited state. In that case the dip will be at half the maximum level.

The qubit's eigenfrequency can be shifted by applying a Stark shift. This is a crucial part that allows to have Jaynes–Cummings (resonant) interactions with the phononic modes and then isolate the qubit at its "rest" frequency for the rest of the experiment. Otherwise there would be constant Rabi oscillations between the two parts.

Once the qubit is identified the following properties are characterized:

- Rabi π–pulse length and power: an excitation pulse is sent to the qubit, followed by the readout pulse. Typically one would vary the duration of the excitation pulse, which would lead to an oscillating readout signal with the form of a cosine since for zero duration (no pulse) the qubit remains at the ground state and the readout is maximized. The first signal minimum corresponds to a π–pulse. Another approach

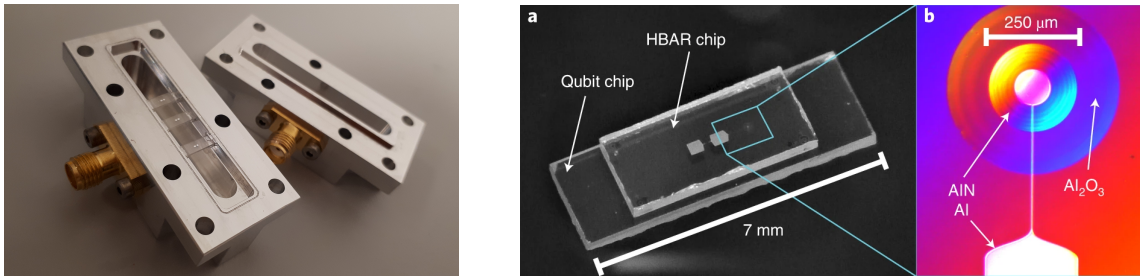

(a) (b)

Figure 5.1: Part of the experimental setup, the microwave cavity along with the samples inside. This microwave cavity is then mounted inside a dilution refrigerator, at the bottom plate. (a) Photograph of the open microwave cavity with three $\hbar$BAR chips glued on the sides. One of the connectors is where the input line ends and the other where the output starts. Photograph from the group's archive. (b) Close–up of the two flip–chip bonded substrates, one for the qubit and one for the HBAR. Image from [23].

is to send a pulse of fixed duration and sweep over the input power for what is called the *power Rabi*, in which case one finds the power that corresponds to a π–pulse.

- T_1: this measurement consists of a π–pulse, sweeping over the waiting time and then a readout pulse. Fitting an exponential decay gives the lifetime of the qubit.

- T_2 and T_2^*: to find the pure spin relaxation time, T_2, meaning the decoherence in the transverse plane of the Bloch sphere excluding the static dephasing from the environment, one performs a Hahn echo experiment[30] with $\pi/2$–pulse, wait time t, π–pulse, another wait time t and finally another $\pi/2$–pulse followed by readout. For the total decoherence, T_2^*, one does a Ramsey experiment, which is the same as the above but without the echo pulse.

The same characterizations can also be done for phonons. First we need to find the frequencies of these modes. This can be done by exciting the qubit and then implementing a Stark–shift to change its frequency, leave it at the new frequency for a certain amount of time and perform readout. A plot of that is shown in Figure 5.2, with the colorbar indicating the readout signal power. If no phonon modes are near the qubit frequency, the signal should have the same behaviour as in the characterization steps of the qubit. This is why for most of the spectrum the signal starts from a lower value, qubit being excited, and as time passes and the qubit decays the signal increases. On the other hand, if there is a phonon mode close–by, then there is going to be some resonant (Jaynes–Cummings) interaction between the two systems and the signal is going to differ. More specifically there will be a faster decay of the qubit as part of the excitation would be transferred to the phonon. With the qubit on resonance with the phonon, a cross–cut along the time delay axis shows decaying oscillations, which correspond to coherent exchanges of an excitation between the qubit and the phonon.

Once the frequency of the mode is found, then the interaction time between the two systems needs to be optimized. The goal is to find the duration for which we get the transition $|e,0\rangle \rightarrow |g,1\rangle$, with the notation indicating $|\text{qubit}, \text{phonon in Fock basis}\rangle$. The introduced excitation performs Rabi oscillation and so for the transition we want the duration of the SWAP gate to be $\tau = \pi/2g$, with g the coupling strength. This factor of 2 comes from the definition of the coupling rate. We write the entangled qubit–phonon state that contains a total of 1 excitation as $\cos(g \cdot t)\,|e,0\rangle + \sin(g \cdot t)\,|g,1\rangle$ and since the signal gives us the qubit state probability, it is proportional to $|\cos(g \cdot t)|^2$, which oscillates with a frequency of $2g$.

At this point everything needed for the phonon mode characterization is available. The example of the phonon T_1 measurement is shown in Figure 5.3, where the vertical distance

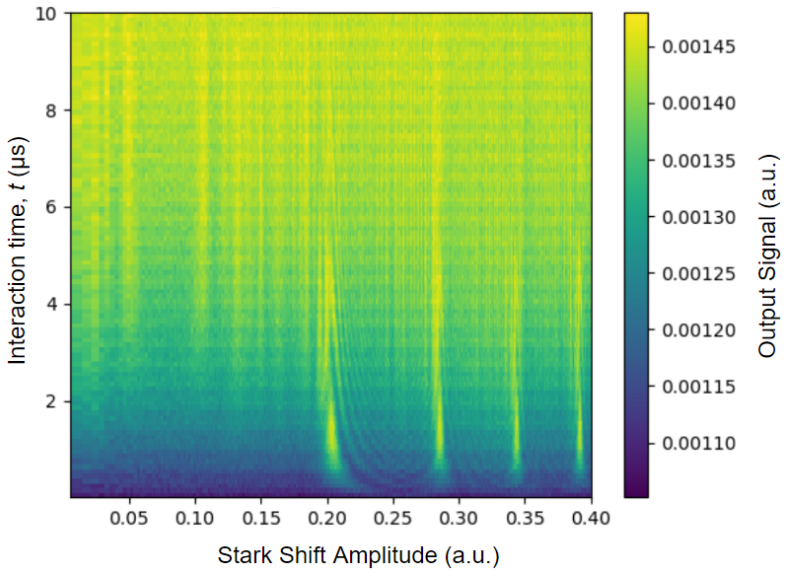

Figure 5.2: 2D phonon Rabi spectrum of device D04 from Table 5.1. The Stark–shift amplitude in the x–axis corresponds directly to the frequency shift induced to the qubit. The frequency and amplitude have a square–root relation and the spectrum we have here has a roughly 30.3 MHz range, from 5.7476 GHz to 5.7779 GHz. The colour bar indicates the power of the readout signal.

between the upper and lower horizontal lines indicates the detuning between the systems. Depending on the sequence one can create more complex phonon states, like a cat state for example[24].

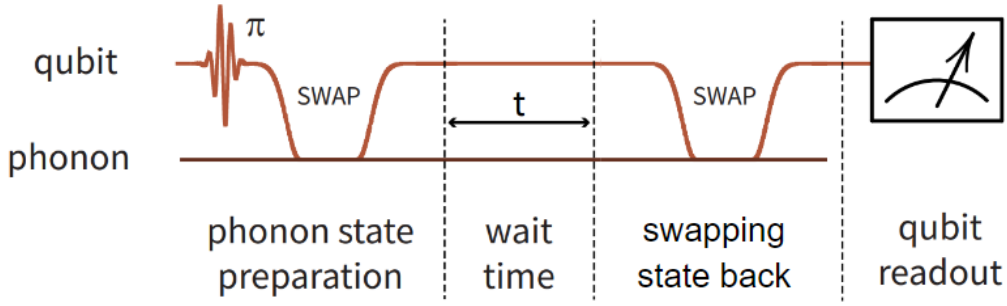

Figure 5.3: Pulse sequence for measuring T_1 for a phonon state.

Since the operations done on the phonons are through the qubit the only measurement not done for the former are the echo pulses, because the in–between π–pulse requires two more excitation swaps and thus is going to be a more lossy operation. All the other characterization steps can also be done for the phonon modes in the context of cQAD.

5.2. Devices

All the Lithium Niobate devices that have been measured in the group so far come from the same wafer, a substrate of 665 µm sapphire on top of which a piezoelectric layer of 900 nm is deposited. This thickness is not ideal for our frequency range and during the fabrication process it was reduced to about 600 nm. In Figure 5.4 we see microscope images and plots from Atomic Force Microscopy (AFM) data for three samples. Two of them have already been measured, dome D_{85} before this thesis started and D_{04} during this thesis. Dome D_{11} is from a wafer of another supplier and is one of the upcoming samples to be measured.

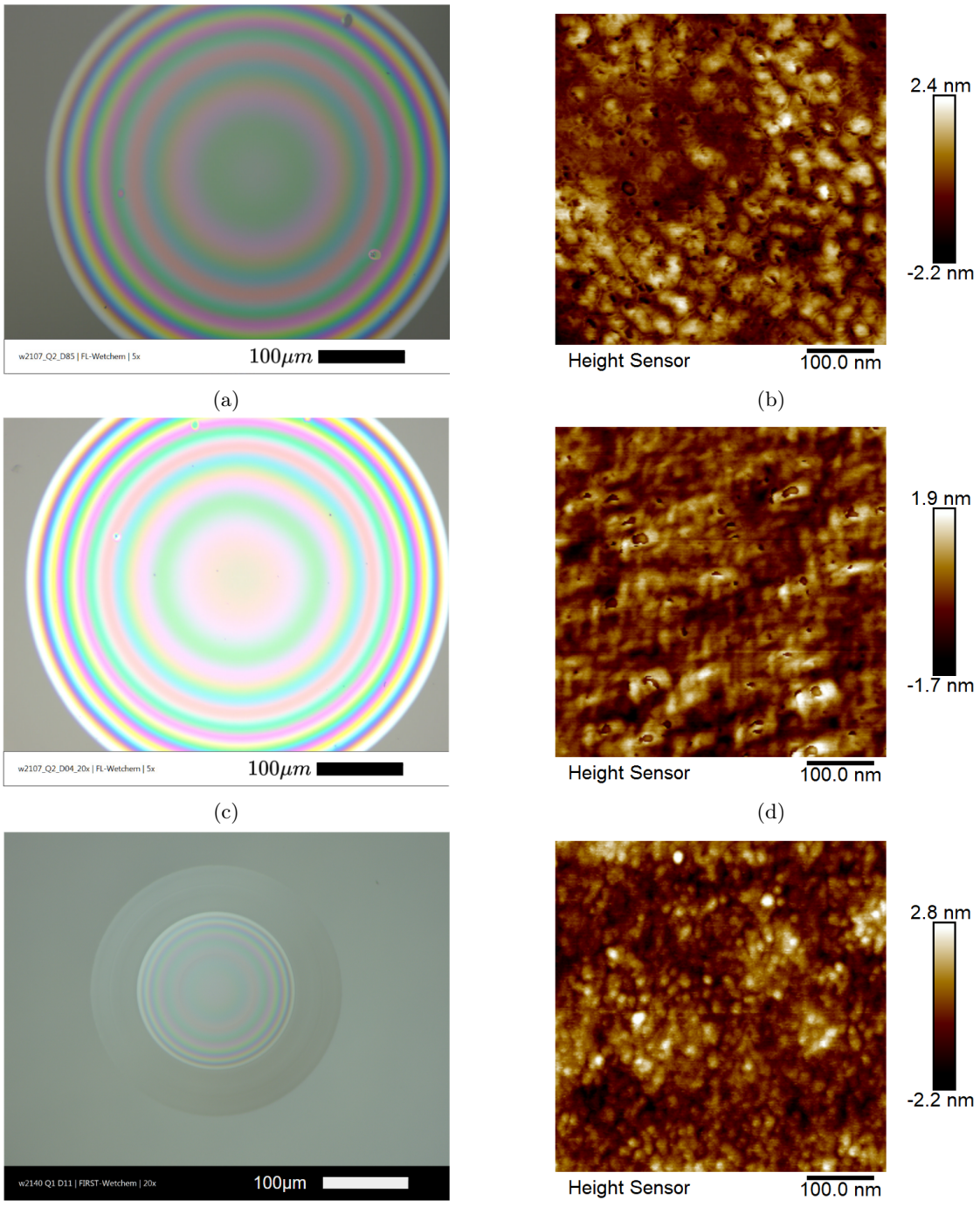

Figure 5.4: Images from microscope and height maps from AFM data for domes D_{85}, D_{04} of table 5.1 and for one of the upcoming samples D_{11}. (a) Microscope image of D_{85}. (b) AFM data of D_{85}. (c) Microscope image of D_{04}. (d) AFM data of D_{04}. (e) Microscope image of D_{11}. (f) AFM data of D_{11}.

From the microscope images we can see the defects that the measured samples had, which come from pinholes in the original Lithium Niobate layer supplied by the manufacturer. The specific ones were chosen because the defects are not in the region of the dome, where the fundamental mode would be. Still however, they could affect the performance, which is summarized in table 5.1. Note that the sharp "holes" in Figures 5.4 (b) and (d) are AFM artifacts, but they do not affect the measured RMS roughness by much. The new samples were made from wafers made by a different supplier. In subfigure (e) the microscope image for D_{11} does not show any signs of such defects anywhere near the dome, which is certainly promising.

5.3. Results

So far there have been two rounds of measurements of a Lithium Niobate $\hbar$BAR, one in March 2022 and one in December 2022. In both cases there were two samples measured, so four in total. Additionally, all of them were from the same wafer which is a Sapphire substrate with Lithium Niobate on top. The dimensions of all samples are roughly the same, summarized at the second row of table 4.1. The only difference is that the first two and the final two samples were bonded to qubits of different fabrication rounds. The results for one of the samples measured in December are presented here. For the qubit the HBAR is bonded to, the readout signal for the T_1, T_2 and T_2^* along with the fitted functions are shown in Figure 5.5.

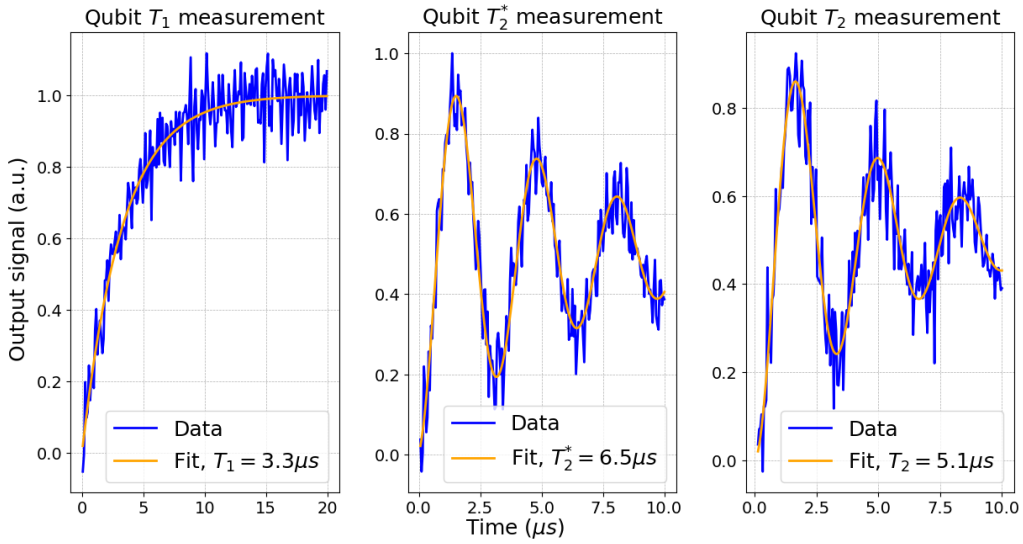

Figure 5.5: Qubit characterization measurements for the qubit bonded to the HBAR with dome D_{04}. From left to right we see the time evolution of the readout signal power for T_1–, T_2– and T_2^*–measurements along with the fitted functions and the extracted values.

We see that the loss rate of the qubit is $\gamma_q = 2\pi \cdot T_1 = 2\pi \cdot 48\,\text{kHz}$. What is strange is that $T_2^* < T_2$. This is probably due to imperfect measurement implementation, like a non–ideal $\pi/2$–pulse or echo pulse.

Using the 2D Rabi sweep shown in Figure 5.2, we find the frequencies of the fundamental HG–00 modes as the frequencies of the most dominant chevron patterns. A zoom–in of one of those is shown on Figure 5.6(a) from which we find the frequency at which the fundamental mode is. From Figure 5.6(b) we can see that the swap time between the two

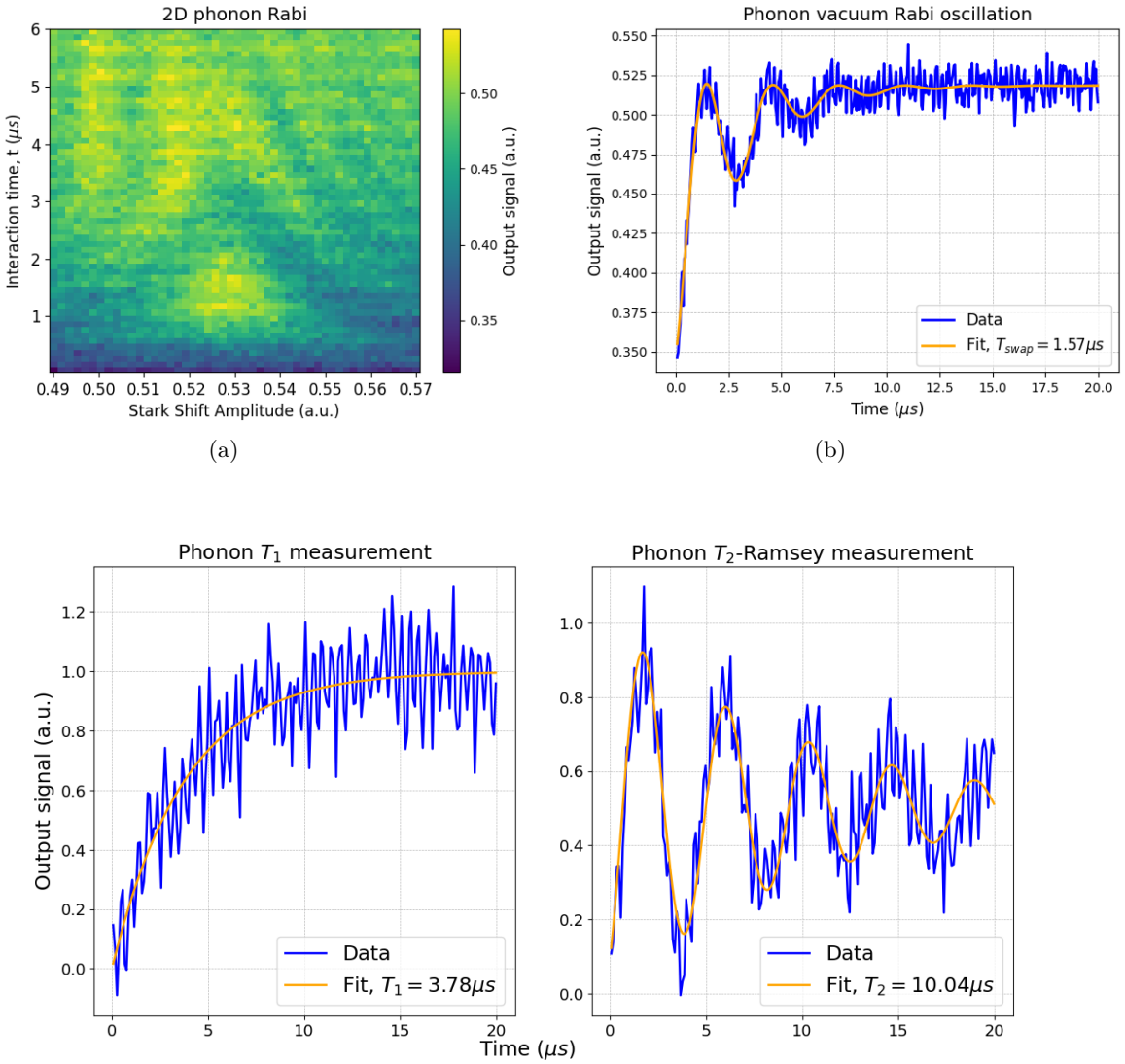

Figure 5.6: Phonon characterization measurements. (a) Close–up of a 2D phonon Rabi scan around a Chevron pattern caused by a phononic mode. This does not come from the sweep shown in Figure 5.2, as the different range in Stark–shift amplitude indicates, but it is from the same sample at a different time. (b) Time evolution of output signal during Rabi oscillation between the two systems, decaying due to the losses of the individual parts. (c) Phonon mode T_1 (left) and T_2 (right) measurements along with the fitted functions and the extracted values.

systems is about $T_{swap} = 1.57$us. From this we estimate the coupling rate as:

$$\frac{g}{2\pi} = \frac{1}{4 * T_{swap}} = 159\,\text{kHz}. \tag{5.1}$$

Then the phonon T_1 was measured as described in the previous section with the results shown in Figure 5.6(c) on the left and for T_2 the phonon Ramsey results on the right. The lifetime is much smaller than what we expect from our BeamProp simulations and we can assume that the high loss rate comes from sources other than diffraction. In addition there seems to be an additional off–resonant oscillation in the signal. We also observe that T_2 is larger than $2 \cdot T_1$ which is the theoretical upper limit.

For dome D_{95} due to the even worse qubit performance we did not proceed with the full phonon characterization.

	Cooldown March 2022		Cooldown December 2022	
Device	D24	D85	D04	D95
qubit T_1(µs)	1.7	0.96	3.3	1
qubit T_2 (µs)	1.2	2.33	5.1	2.2
qubit T_2^* (µs)	1.06	1.47	6.5	1.4
phonon T_1 (µs)	3.98	10.52	3.78	-
phonon T_2 (µs)	2.6	18.36	10.04	-
$g/2\pi$ (kHz)	180	200	159	-

Table 5.1.: Measured values for qubits and phonon of Lithium Niobate ħBARs. All these devices are from the same 665 µm Lithium Niobate on Sapphire substrate. The measurements were done in the cooldowns written on the first row.

In terms of coupling rates the results were approximately as expected, considering equation 4.2. Regarding phonon characterization, as stated in section 4.3 the lifetimes do not agree with the simulations. However, since all the measured samples come from the same substrate it is possible that losses are substrate–specific. Once more measurements with Lithium Niobate samples are done we will have more information to help us draw conclusions.

Chapter 6

Discussion and Outlook

The work of this thesis has been on (i) mostly BeamProp in two directions: expanding the 1D case to include reflections, implementing the 3D case, (ii) COMSOL simulations for the upcoming sample and (iii) performing measurements of $LiNbO_3$ HBARs coupled to qubits.

In terms of phonon dissipation it seems that (at least for the measured samples) diffraction losses are not the main decay mechanism of our devices. Some other factors that may be the root for decay are phonon–phonon, phonon–defect and surface scattering. We believe that the reason was in the end the specific sample, the wafer used for the fabrication of these HBARs. This could originate from the holes on the dome, even though for the samples used those were not in the dome region where the mechanical mode would "live". There could still be material impurities present in the bulk that lead to dissipation.

The measurements of the new Lithium Niobate devices will help us come to further conclusions. Microscope images, AFM and profilometer measurements of the surface roughness show that these new devices have very good surfaces. The following cases and the information they would provide are:

- if both new samples have very high losses then we can exclude the role of the large pinhole defects and would still need to find the decaying factor.
- If both samples have good and very similar lifetimes, below the limit set by BeamProp3D then the implementation of this part has been wrong.
- If *New LN 1* outperforms *New LN 2* then it is quite likely that the smaller RoC of the latter and hence the smaller area under the dome led to that. So in this scenario, fabricating a sample from the same wafer but with higher RoC would correct for polarization–conversion–related diffraction losses.

After that, what would also be interesting and extremely important for operating in the strong coupling regime is to investigate whether the piezoelectric material plays a role in the low qubit lifetimes our samples have had for a while. This performance is ascribed to dielectric losses. It could be that due to Lithium Niobate's coupling matrix elements there is an increased coupling to phonons propagating in x– and y–direction.

If the lifetimes of the upcoming samples are better, then there are still two situations in which Lithium Niobate can be used instead of Aluminum Nitride. One is driving shear phononic modes with higher coupling rates. If we look at the last three columns of AlN's piezoelectric tensor it has elements with much lower value, so g would be low as well. Finally, another case would be using a different material cut to drive longitudinal modes in z using one of the transverse (E_x for example) electric field components in cases where using E_z might not be an option.

BeamProp3D implementation

In the description of the BeamProp algorithm there was no mention of how information regarding the slowness surfaces is acquired. The whole simulation software is written in *Python* and the *Christoffel* module is used[i]. The way this module is used is that you input the stiffness tensor and density of the material of interest and it creates an object. One can use this object by, for example, setting a direction within the material and retrieving the eigenvalues and eigenvectors of the Christoffell equation in this direction.

So if one sets the direction as $\hat{n} = (n_x, n_y, n_z)$ and gets the phase–velocity eigenvalues ν_{t_1}, ν_{t_2} and ν_l, then the coordinates of the slowness surfaces in that direction are:

$$\begin{aligned} [q_{x,t_1}, q_{y,t_1}, q_{z,t_1}] &= [n_x/\nu_{t_1}, n_y/\nu_{t_1}, n_z/\nu_{t_1}] \\ [q_{x,t_2}, q_{y,t_2}, q_{z,t_2}] &= [n_x/\nu_{t_2}, n_y/\nu_{t_2}, n_z/\nu_{t_2}] \\ [q_{x,l}, q_{y,l}, q_{z,l}] &= [n_x/\nu_l, n_y/\nu_l, n_z/\nu_l], \end{aligned} \tag{A.1}$$

with $\underline{q}$ the slowness vectors and the indices referring to the components of those vectors and which of the surfaces they describe.

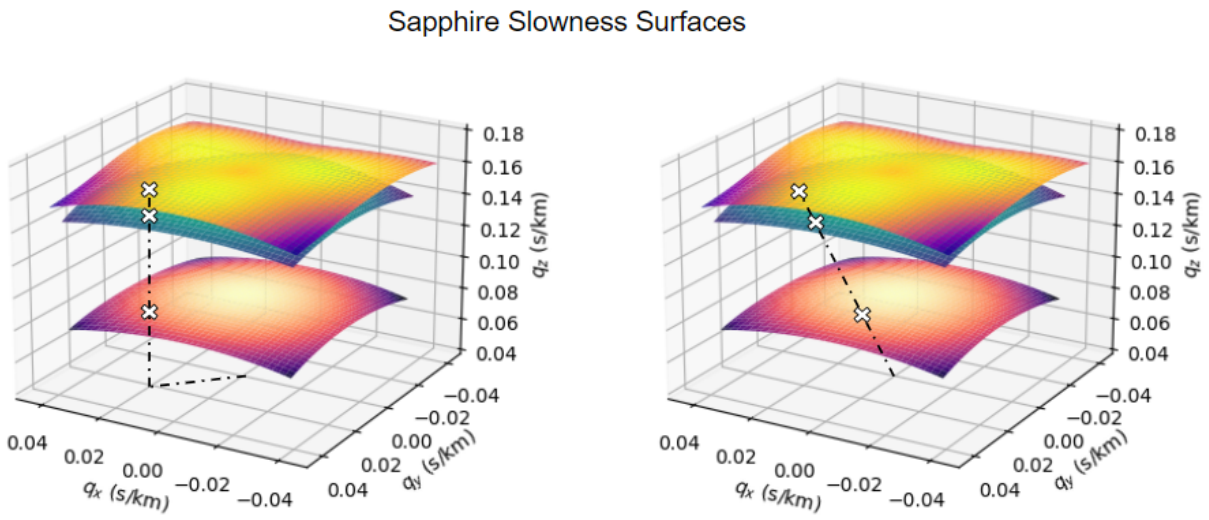

Figure A.1: Slowness surfaces of Sapphire about the $[0, 0, 1]$ direction along with information regarding the 3D BeamProp implementation. On the left, the lines indicate that in BeamProp we want the q_z for given q_x and q_y. On the right we see the results from the Christoffell module, which finds the eigenvalues for a given direction.

Figure A.1 helps to visualize the issue. In BeamProp we have two coordinates of the slowness surfaces for every frequency, which are $[q_x, q_y] = [k_x/\omega, k_y/\omega]$ and are looking for the third. The available tool does not give this capability.

The solution that was applied is to set a grid of many different directions, get the eigenvalues for each one and thus have a collection of coordinates for each slowness surface. Then these coordinates are used to create an interpolator object with $input = [q_x, q_y]$ and

[i] https://github.com/JanJaeken/christoffel

$output = [q_z]$. This object can then be used by the known values of $[q_x, q_y]$ in BeamProp in order to obtain the three q_z^i values for the three slowness surfaces.

After different interpolation options the one that is used in the end is the NearestNDInterpolator from *scipy*[ii].The main advantage in that case is that interpolators can also be used for the polarization vectors instead of being calculated on the spot. So now $output = [q_z, d_x, d_y, d_z]$ for each surface, leading to a total of twelve interpolators.

Another benefit is that in other interpolation methods, two (for linear interpolation) or more points are being used. The polarization vectors however can have very sudden changes, which is something that holds specifically for the quasi–transverse slowness surfaces in Sapphire. This can be seen in more detail in Figure 3.3. On the slowest surface for sapphire for example (top left subplot) we see that in the region $q_x \approx 0$ and $q_y > 0$ the polarization vectors have a sudden change from pointing to the right (as the $[1, 0]$ vector) to pointing to the left (as the $[-1, 0]$ vector). The average of points at the boarder of that sudden polarization change would give $d_x = 0$ which would be wrong. Similarly there are regions where the polarization vectors turn from mainly x–polarized to mainly y–polarized.

[ii] https://docs.scipy.org/doc/scipy/reference/generated/scipy.interpolate.NearestNDInterpolator.html#scipy.interpolate.NearestNDInterpolator

Material Parameters

The form of the tensors that describe the behaviour of materials depends on their structure[19]. The stiffness tensor, c_{ijkl}, as a 4th–rank tensor which would normally have 81 independent components. Due to the symmetries of the strain and stress tensors they get reduced to 36. Then through further thermodynamic considerations their number reduces to 21. From that point, the symmetry of the crystalline structure also affects the number of independent elements.

B.1. Sapphire–Al_2O_3

Sapphire has trigonal crystal symmetry, which leads to the following form of its stiffness tensor in Voigt notation [17]:

$$c_{\alpha\beta} = \begin{pmatrix} c_{11} & c_{12} & c_{13} & c_{14} & 0 & 0 \\ c_{12} & c_{11} & c_{13} & -c_{14} & 0 & 0 \\ c_{13} & c_{13} & c_{33} & 0 & 0 & 0 \\ c_{14} & -c_{14} & 0 & c_{44} & 0 & 0 \\ 0 & 0 & 0 & 0 & c_{44} & c_{14} \\ 0 & 0 & 0 & 0 & c_{14} & \frac{c_{11}-c_{12}}{2} \end{pmatrix}. \tag{B.1}$$

From the Handbook of Constants[31] we get the values $c_{11} = 496\,\text{GPa}$, $c_{12} = 159\,\text{GPa}$, $c_{13} = 114\,\text{GPa}$, $c_{14} = -23\,\text{GPa}$, $c_{33} = 499\,\text{GPa}$ and $c_{44} = 146\,\text{GPa}$.

B.2. Aluminum Nitride–AlN

AlN has hexagonal symmetry with stiffness tensor:

$$c_{\alpha\beta} = \begin{pmatrix} c_{11} & c_{12} & c_{13} & 0 & 0 & 0 \\ c_{12} & c_{11} & c_{13} & 0 & 0 & 0 \\ c_{13} & c_{13} & c_{33} & 0 & 0 & 0 \\ 0 & 0 & 0 & c_{44} & 0 & 0 \\ 0 & 0 & 0 & 0 & c_{44} & 0 \\ 0 & 0 & 0 & 0 & 0 & \frac{c_{11}-c_{12}}{2} \end{pmatrix} \tag{B.2}$$

where $c_{11} = 376\,\text{GPa}$, $c_{12} = 129\,\text{GPa}$, $c_{13} = 98\,\text{GPa}$ and $c_{33} = 353\,\text{GPa}$ [32]. As a piezoelectric material it has matrix of piezoelectric constants:

$$d = \begin{pmatrix} 0 & 0 & 0 & 0 & d_{15} & 0 \\ 0 & 0 & 0 & d_{15} & 0 & 0 \\ d_{31} & d_{31} & d_{33} & 0 & 0 & 0 \end{pmatrix} \tag{B.3}$$

with $d_{31} = -2.8\,\text{pm/V}$, $d_{33} = 5.6\,\text{pm/V}$ and $d_{15} = 3.6\,\text{pm/V}$ as in [33] (values for bulk AlN) and [34]. These two tensors are combined to get the piezoelectric coupling tensor

$e = d \cdot c$:

$$e = \begin{pmatrix} 0 & 0 & 0 & 0 & e_{15} & 0 \\ 0 & 0 & 0 & e_{15} & 0 & 0 \\ e_{31} & e_{31} & e_{33} & 0 & 0 & 0 \end{pmatrix} \tag{B.4}$$

with $e_{31} = -0.86\,\mathrm{C/m^2}$, $e_{33} = 1.43\,\mathrm{C/m^2}$ and $e_{15} = 0.41\,\mathrm{C/m^2}$. For the orientation of the material and the electric field in the $\hbar$BARs case the most important of these numbers is e_{33}, which couples a z–oriented E–field to S_3 strain.

B.3. Lithium Niobate–$LiNbO_3$

Lithium Niobate also has trigonal symmetry and so its stiffness tensor is given by equation B.1 with $c_{11} = 202\,\mathrm{GPa}$, $c_{12} = 55\,\mathrm{GPa}$, $c_{13} = 72\,\mathrm{GPa}$, $c_{14} = 8.5\,\mathrm{GPa}$, $c_{33} = 244\,\mathrm{GPa}$ and $c_{44} = 60.2\,\mathrm{GPa}$ [31]. The piezoelectric coupling tensor has the form:

$$e = \begin{pmatrix} 0 & 0 & 0 & 0 & e_{15} & -e_{22} \\ -e_{22} & e_{22} & 0 & e_{15} & 0 & 0 \\ e_{31} & e_{31} & e_{33} & 0 & 0 & 0 \end{pmatrix} \tag{B.5}$$

with $e_{15} = 3.83\,\mathrm{C/m^2}$, $e_{22} = 2.37\,\mathrm{C/m^2}$, $e_{31} = 0.23\,\mathrm{C/m^2}$ and $e_{33} = 1.3\,\mathrm{C/m^2}$ [35]. Performing a rotation about the X-axis by 90°, so that the Y–axis is in the initially Z–direction, rotates the tensor such that:

$$e_{\text{Y-cut}} = \begin{pmatrix} 0 & 0 & 0 & 0 & 2.37 & 3.83 \\ -0.23 & -1.3 & -0.23 & 0 & 0 & 0 \\ -2.37 & 0 & 2.37 & 3.83 & 0 & 0 \end{pmatrix}. \tag{B.6}$$

Bibliography

1. Acın, A. *et al.* The quantum technologies roadmap: a European community view. *New Journal of Physics* **20,** 080201. https://doi.org/10.1088/1367-2630/aad1ea (Aug. 2018).
2. Blais, A., Grimsmo, A. L., Girvin, S. M. & Wallraff, A. Circuit Quantum Electrodynamics. https://arxiv.org/abs/2005.12667 (2020).
3. Bruzewicz, C. D., Chiaverini, J., McConnell, R. & Sage, J. M. Trapped-ion quantum computing: Progress and challenges. *Applied Physics Reviews* **6,** 021314. https://doi.org/10.1063/1.5088164 (June 2019).
4. Wang, J., Sciarrino, F., Laing, A. & Thompson, M. G. Integrated photonic quantum technologies. *Nature Photonics* **14,** 273–284. https://doi.org/10.1038/s41566-019-0532-1 (Oct. 2019).
5. Lahtinen, V. & Pachos, J. K. A Short Introduction to Topological Quantum Computation. https://arxiv.org/abs/1705.04103 (2017).
6. Burkard, G., Ladd, T. D., Nichol, J. M., Pan, A. & Petta, J. R. *Semiconductor Spin Qubits* 2021. https://arxiv.org/abs/2112.08863.
7. Chu, Y. & Gröblacher, S. A perspective on hybrid quantum opto- and electromechanical systems. *Applied Physics Letters* **117,** 150503. https://doi.org/10.1063/5.0021088 (Oct. 2020).
8. Chu, Y. *et al.* Quantum acoustics with superconducting qubits. *Science* **358,** 199–202. https://doi.org/10.1126/science.aao1511 (Oct. 2017).
9. Manenti, R. *et al.* Circuit quantum acoustodynamics with surface acoustic waves. *Nature Communications* **8.** https://doi.org/10.1038/s41467-017-01063-9 (Oct. 2017).
10. Chu, Y. *et al.* Creation and control of multi-phonon Fock states in a bulk acoustic-wave resonator. *Nature* **563,** 666–670. https://doi.org/10.1038/s41586-018-0717-7 (Nov. 2018).
11. MacCabe, G. S. *et al.* Nano-acoustic resonator with ultralong phonon lifetime. *Science* **370,** 840–843. https://doi.org/10.1126/science.abc7312 (Nov. 2020).
12. Rosso, P. *Engineering Eigenstates in High-Overtone Bulk Acoustic Resonators* MA thesis (ETH Zurich, Zurich, Switzerland, 2022).
13. Sletten, L., Moores, B., Viennot, J. & Lehnert, K. Resolving Phonon Fock States in a Multimode Cavity with a Double-Slit Qubit. *Physical Review X* **9.** https://doi.org/10.1103/physrevx.9.021056 (June 2019).
14. Schliesser, A., Rivière, R., Anetsberger, G., Arcizet, O. & Kippenberg, T. J. Resolved-sideband cooling of a micromechanical oscillator. *Nature Physics* **4,** 415–419. https://doi.org/10.1038/nphys939 (Apr. 2008).
15. Arrangoiz-Arriola, P. *et al.* Resolving the energy levels of a nanomechanical oscillator. *Nature* **571,** 537–540. https://doi.org/10.1038/s41586-019-1386-x (July 2019).
16. Renninger, W. H., Kharel, P., Behunin, R. O. & Rakich, P. T. Bulk crystalline optomechanics. *Nature Physics* **14,** 601–607. https://doi.org/10.1038/s41567-018-0090-3 (Apr. 2018).
17. Cleland, A. N. *Foundations of Nanomechanics* https://doi.org/10.1007/978-3-662-05287-7 (Springer Berlin Heidelberg, 2003).

18. Scully, M. O. & Zubairy, M. S. *Quantum Optics* https://doi.org/10.1017/cbo9780511813993 (Cambridge University Press, Sept. 1997).

19. Royer, D. & Dieulesaint, E. *Elastic waves in solids I* 2nd ed. en (Springer, Berlin, Germany, Nov. 1999).

20. Newberry, B. P. & Thompson, R. B. A paraxial theory for the propagation of ultrasonic beams in anisotropic solids. *The Journal of the Acoustical Society of America* **85,** 2290–2300. https://doi.org/10.1121/1.397775 (June 1989).

21. Jain, V. *et al. Acoustic radiation from a superconducting qubit: From spontaneous emission to Rabi oscillations* 2022. https://arxiv.org/abs/2211.07475.

22. Banderier, H., Drimmer, M. & Chu, Y. *Unified simulation methods for quantum acoustic devices* 2023. eprint: arXiv:2301.05172.

23. Von Lüpke, U. *et al.* Parity measurement in the strong dispersive regime of circuit quantum acoustodynamics. *Nature Physics* **18,** 794–799. https://doi.org/10.1038/s41567-022-01591-2 (May 2022).

24. Bild, M. *et al. Schrödinger cat states of a 16-microgram mechanical oscillator* 2022. https://arxiv.org/abs/2211.00449.

25. Schrinski, B. *et al.* Macroscopic Quantum Test with Bulk Acoustic Wave Resonators. *Physical Review Letters* **130.** https://doi.org/10.1103/physrevlett.130.133604 (Mar. 2023).

26. Von Lüpke, U., Rodrigues, I. C., Yang, Y., Fadel, M. & Chu, Y. *Engineering phonon-phonon interactions in multimode circuit quantum acousto-dynamics* 2023. https://arxiv.org/abs/2303.00730.

27. Saleh, B. E. A. & Teich, M. C. *Fundamentals of Photonics* https://doi.org/10.1002/0471213748 (John Wiley & Sons, Inc., Aug. 1991).

28. *Optique-ingenieur.org* http://www.optique-ingenieur.org/en/courses/OPI_ang_M01_C03/co/Contenu_13.html.

29. Krantz, P. *et al.* A quantum engineer's guide to superconducting qubits. *Applied Physics Reviews* **6,** 021318. https://doi.org/10.1063/1.5089550 (June 2019).

30. Levitt, M. *Spin Dynamics: Basics of Nuclear Magnetic Resonance* ISBN: 9781118681848. https://books.google.ch/books?id=bysFAa4MPQcC (Wiley, 2013).

31. *Springer Handbook of Condensed Matter and Materials Data* (eds Martienssen, W. & Warlimont, H.) https://doi.org/10.1007/3-540-30437-1 (Springer Berlin Heidelberg, 2005).

32. De Jong, M. *et al.* Charting the complete elastic properties of inorganic crystalline compounds. *Scientific Data* **2.** https://doi.org/10.1038/sdata.2015.9 (Mar. 2015).

33. Guy, I. L., Muensit, S. & Goldys, E. M. Extensional piezoelectric coefficients of gallium nitride and aluminum nitride. *Applied Physics Letters* **75,** 4133–4135. https://doi.org/10.1063/1.125560 (Dec. 1999).

34. Muensit, S., Goldys, E. M. & Guy, I. L. Shear piezoelectric coefficients of gallium nitride and aluminum nitride. *Applied Physics Letters* **75,** 3965–3967. https://doi.org/10.1063/1.125508 (Dec. 1999).

35. Warner, A. W., Onoe, M. & Coquin, G. A. Determination of Elastic and Piezoelectric Constants for Crystals in Class (3im/i). *The Journal of the Acoustical Society of America* **42,** 1223–1231. https://doi.org/10.1121/1.1910709 (Dec. 1967).

Eidgenössische Technische Hochschule Zürich
Swiss Federal Institute of Technology Zurich

Declaration of originality

The signed declaration of originality is a component of every semester paper, Bachelor's thesis, Master's thesis and any other degree paper undertaken during the course of studies, including the respective electronic versions.

Lecturers may also require a declaration of originality for other written papers compiled for their courses.

I hereby confirm that I am the sole author of the written work here enclosed and that I have compiled it in my own words. Parts excepted are corrections of form and content by the supervisor.

Title of work (in block letters):

Characterization of Lithium Niobate for High–Overtone Bulk Acoustic Wave Devices

Authored by (in block letters):

For papers written by groups the names of all authors are required.

Name(s):	**First name(s):**
Pappas	Angelos

With my signature I confirm that

- I have committed none of the forms of plagiarism described in the 'Citation etiquette' information sheet.
- I have documented all methods, data and processes truthfully.
- I have not manipulated any data.
- I have mentioned all persons who were significant facilitators of the work.

I am aware that the work may be screened electronically for plagiarism.

Place, date	**Signature(s)**
Zurich, 26.06.2023	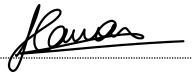

For papers written by groups the names of all authors are required. Their signatures collectively guarantee the entire content of the written paper.